



DEGREE PROJECT IN MATERIALS SCIENCE AND ENGINEERING,  
SECOND CYCLE, 30 CREDITS  
*STOCKHOLM, SWEDEN 2020*

# **The Effect of Cooling Rate on Sintered Cemented Carbides**

**LINA BERGLUND**



**KTH ROYAL INSTITUTE OF TECHNOLOGY  
SCHOOL OF INDUSTRIAL ENGINEERING AND MANAGEMENT**

---

## Abstract

Magnetic measurements are useful tools for quality control of cemented carbides. Previous work at Sandvik Mining and Rock Technology has shown that the coercivity increases with increased cooling rate during sintering for a specific grade. This study aims to investigate why the coercivity changes with the cooling rate and if this is true for other cemented carbide grades as well. Three different cemented carbide grades were sintered with different cooling rates and evaluated with coercivity, Cobalt-magnetic saturation and hardness measurements, and with microscopy and Electron Backscatter Diffraction analysis.

It was found that the coercivity increased with increasing cooling rates for the previously studied grade, but not for the two other grades. It was expected that the increased coercivity would indicate a decrease in WC grain size, but the results showed that the WC grain size of the fastest and slowest cooling rate were the same. However, a change in size of the Co areas between the WC grains was found. The fast cooled sample showed smaller Co areas than the slow cooled sample. These Co/WC grain boundaries increase the coercivity. An increased fraction of hcp-Co/fcc-Co was also found for the fast cooled material which also increases the coercivity.

No relationship between the hardness and the coercivity or the cooling rate was found. The contiguity for the different grades was also calculated. No significant difference in contiguity between the different cooling rates of each material was found but the contiguity values between the different materials differed. This is probably mainly dependent on the different binder contents of the materials.

Keywords: *Sintering; Cooling rate; Cemented Carbide; Sintering; Coercivity; Contiguity*

---

## Sammanfattning

Magnetiska egenskaper är en viktig del av kvalitetskontrollen av hårdmetaller. Tidigare forskning hos Sandvik Mining and Rock Technology har visat att koerciviteten hos en hårdmetallsort ökar med ökad kylhastighet vid sintring. Målet med den här studien är att undersöka varför koerciviteten ökar med kylhastigheten och om detta även gäller andra hårdmetallsorter. Tre olika hårdmetallsorter sintrades med olika kylhastigheter undersöktes med mätningar av koercivitet, magnetisk mätnat i koboltfasen och hårdhet, samt med mikroskopi och Electron Backscatter Diffraction analys.

Det visade sig att koerciviteten ökade med ökad kylhastighet för hårdmetallsorten som studerats tidigare, men inte för de andra två sorterna. En ökad koercivitet förväntas visa på en minskad WC-kornstorlek, men resultaten visar att det långsamt kylda och snabbkylda provet hade samma WC-kornstorlek. Däremot upptäcktes en ändring av storleken på Co-områdena mellan WC-kornen. Det snabbkylda provet visade en mindre storlek av Co-områdena jämfört med det långsamt kylda provet. Fler Co/WC-korngränser i det snabbkylda provet leder till en ökad koercivitet. Fraktionen av hcp-Co/fcc-Co-korngränser ökade också för det snabbkylda provet vilket också ökar koerciviteten.

Inget samband mellan hårdheten och koerciviteten eller kylhastigheten upptäcktes. Beräkning av kontiguiteten för de olika sorterna genomfördes också. Ingen signifikant skillnad i koercivitet mellan de olika kylhastigheterna för the olika sorterna hittades, men kontiguiteten mellan de olika sorterna varierade. Det beror mest troligt på att dom olika sorterna har olika mängd matris-material.

Nyckelord: *Sintring; Kylhastighet; Hårdmetaller; Koercivitet; Kontiguitet*

---

## Abbreviations

Co	Cobalt
WC	Tungsten carbide
Cr	Chromium
fcc	Face centered cubic crystal structure
hcp	Hexagonal close packed crystal structure
Hc	Coercivity
Co-m	Cobalt-magnetic saturation
HV20	Vickers hardness with a load of 20 kg
$C_{WC}$	Contiguity of the WC grains
$V_{Co}$	Volume fraction of cobalt binder
$x(fcc,W)$	Mole fraction of tungsten dissolved in fcc-Co
SEM	Scanning Electron Microscope
FEGSEM	Scanning Electron Microscope with a Field Emission Gun
EBSD	Electron Backscatter Diffraction
EDS	Energy-Dispersive X-ray Spectroscopy
IPF	Inverse Pole Figure



## Contents

<b>1</b>	<b>Introduction</b>	<b>1</b>
1.1	Aim . . . . .	1
<b>2</b>	<b>Cemented Carbide</b>	<b>2</b>
2.1	Production Process . . . . .	2
2.1.1	Sintering . . . . .	3
2.2	Microstructure . . . . .	4
2.2.1	Grain Size . . . . .	6
2.2.2	Contiguity . . . . .	7
<b>3</b>	<b>Characterization of Cemented Carbides</b>	<b>8</b>
3.1	Hardness . . . . .	8
3.2	Magnetic Measurements . . . . .	8
3.2.1	Coercivity . . . . .	8
3.2.2	Cobalt Magnetic Saturation . . . . .	9
3.3	Microscopy . . . . .	10
3.3.1	Light Optical Microscopy . . . . .	10
3.3.2	Scanning Electron Microscopy . . . . .	10
3.3.3	Electron Backscatter Diffraction . . . . .	10
3.3.4	Energy-Dispersive X-ray Spectroscopy . . . . .	11
3.4	Grain Size Determination . . . . .	11
3.5	Contiguity Determination . . . . .	12
<b>4</b>	<b>Method</b>	<b>13</b>
4.1	Material and Sintering . . . . .	13
4.2	Sample preparation . . . . .	14
4.3	Vickers Hardness . . . . .	14
4.4	Magnetic Measurements . . . . .	14
4.5	Microscopy . . . . .	15
4.6	Contiguity calculations . . . . .	15
4.7	Electron Backscatter Diffraction Analysis . . . . .	15
4.7.1	Grain Size Distribution Evaluation . . . . .	16
4.8	Thermodynamic Calculations . . . . .	17
<b>5</b>	<b>Results</b>	<b>18</b>
5.1	Magnetic Properties and Hardness . . . . .	18
5.2	Microstructure . . . . .	22
5.2.1	Phase Observation . . . . .	22
5.2.2	Grain Size Distribution . . . . .	23
5.2.3	Contiguity . . . . .	32
5.3	Thermodynamic Calculations . . . . .	33

CONTENTS

---

<b>6</b>	<b>Discussion</b>	<b>35</b>
6.1	Sources of Error . . . . .	38
6.2	Sustainability Aspect . . . . .	39
<b>7</b>	<b>Conclusions</b>	<b>40</b>
<b>8</b>	<b>Future Work</b>	<b>41</b>
<b>9</b>	<b>Acknowledgement</b>	<b>42</b>
<b>10</b>	<b>References</b>	<b>43</b>
	<b>Appendix A - Magnetic measurements</b>	<b>46</b>
	<b>Appendix B - Vickers hardness values</b>	<b>48</b>
	<b>Appendix C - Contiguity values</b>	<b>49</b>

# 1 Introduction

Sandvik Mining and Rock Technology (SMRT) is a business area within the Sandvik Group and is a global leading supplier of equipment and technical solutions for the mining and construction industries. Among other things, SMRT produces drill bits and rotating heads for rock excavation. The drill bits are made of steel with inserts made of cemented carbide which is produced by powder metallurgy.

Cemented carbides are one of the most widespread powder metallurgy products and are used worldwide. The main advantage of cemented carbides is that by selecting the appropriate raw materials, compositions, and processing parameters, a wide combination of microstructures and mechanical properties can be achieved. The properties of cemented carbides are determined by the combination of components with significantly different properties, i.e. a tough and soft Co-based binder with hard tungsten carbide (WC) or cubic carbides (e.g. TiC).

Already in 1923, the first patents using cemented carbides were issued by a German company for a method developed by K. Schröter to produce hard material by pressing and sintering [1]. At this time, WC was sintered together with a binder metal such as Fe, Ni and Co in order to produce a solid material. The first cemented carbide of WC and Co was marketed worldwide in 1927 by the German company Friedrich Krupp. It was initially used for wear-resistant parts and wire drawing dies. Cubic carbides, such as TiC, were added to improve the mechanical properties of the cemented carbide.

The combination of hardness and toughness make cemented carbides very attractive for many industrial applications. The global production of cemented carbides has grown rapidly in the past 30 years and today, cemented carbides make up around 50% of the total world market of hard materials. Around 65% of the total cemented carbide market share is related to metal cutting tools, 15% is related to mining, oil drills and rock industries while wood and construction industries account for around 10% [1].

## 1.1 Aim

Research and development is a very important part of the work at SMRT. Previous research within SMRT has shown that different furnaces yielded different coercivity values for the same material. By varying different sintering parameters it was found that the cooling rate had the most significant effect on the coercivity. The coercivity is an indirect measurement of the grain size and a high coercivity value would indicate a fine-grained microstructure that yields higher hardness than a coarse-grained material. The main aim of this study is to investigate why the coercivity changes with the cooling rate for this grade and if the same behaviour can be found for other cemented carbide grades as well.

## 2 Cemented Carbide

Cemented carbides are widely used as cutting and mining tools and for many other wear applications due to the unique combination of hardness, fracture toughness and wear resistance [2]. Most commercial cemented carbides are based on tungsten carbide (WC) and cobalt (Co) but cemented carbides based on other elements also exist. The hard WC grains together with the tough binder phase (most often Co-rich) form a composite structure with unique properties of high hardness and wear resistance [3], [4]. The binder phase is sometimes alloyed with chromium (Cr) to improve the corrosion resistance and as a grain growth inhibitor [5]. In cutting applications, additions of cubic carbides, such as TiC and NbC, improves the high-temperature properties.

Cemented carbides are characterized by high hardness and high compression strength. The elastic moduli for cemented carbides are also high in comparison to steels [4]. The properties of the cemented carbide are mainly influenced by the WC composition, WC grain size, and the amount of binder phase. A large variety of cemented carbides with different WC grain sizes, amounts of binder phase, and WC compositions are produced today. Cemented carbides often consist of 50-95 vol.% WC. The WC grains are prismatically shaped in the sintered material due to the anisotropy of the hexagonal carbide. The fine-grained cemented carbides often have a grain size around 0.8  $\mu\text{m}$  and 3-10 wt% Co. More coarse-grained cemented carbides have a WC grain size between 1 to 10  $\mu\text{m}$  and around 30-40 wt% Co. However, the most common cemented carbides have between 6-10 wt% Co.

### 2.1 Production Process

Cemented carbides are produced by a complex powder metallurgy process which includes many processing steps, such as raw powder production, mixing and milling, spray drying, pressing, sintering, post sintering treatment, and finishing operations [1], [4]. All manufacturing processes are linked; hence, a change in any process step will influence the following process and the quality of the final product [1]. Powder metallurgy makes it possible to manufacture components from hard-to-melt materials such as W. Another significant advantage with powder metallurgy is the manufacturing of products that are difficult to further process when finished, since powder metallurgy provides production of components in a near-net shape. It may also be possible to achieve microstructures with better strength properties compared to what is possible with other methods, since variations in density of the components may cause segregation when melted, and low solubility makes it very difficult to produce homogeneous solution phases. This is the case for cemented carbides. However, with powder metallurgy it is possible to obtain a homogeneous microstructure with acceptable mechanical properties [4].

The production of cemented carbides starts with the milling of the component powders using wet milling with acetone or alcohol and cemented carbides as grinding medium. A compaction aid (often paraffin wax or polyethylene glycol) is added during milling. This makes the fine-grained materials agglomerate, resulting in satisfactory flow and compaction properties of the powder. After milling, the powder is spray-dried in hot nitrogen which vaporizes the milling

liquid leading to spherical agglomerates of carbide and Co particles bound together by the compaction aid. The powder is then pressed by uniaxial or multiaxial compaction forming green bodies. The pressed products are then sintered in a furnace to obtain nearly full density products [4].

### 2.1.1 Sintering

The densification and the microstructural evolution takes place during the sintering process [6]. Sintering is the most important processing step in terms of adjusting the microstructure and mechanical properties of cemented carbides [1]. The sintering process usually includes two stages; debinding of the compaction aid and liquid phase sintering [4], [6]. Both steps are often performed in the same furnace but for some complicated shapes, it is beneficial to perform the debinding step in a separate furnace. A schematic temperature-time curve for sintering is shown in Figure 1. The debinding step takes place at a relatively low-temperature range of 300-400 °C and hydrogen gas is blown into the furnace to improve the debinding of the compaction aid [4]. The compaction aid is burned off and some impurities adsorbed in the powder surface are eliminated [6]. After the debinding step, the temperature is gradually raised to sintering temperature, often between 1350-1500°C. At this temperature, all the Co is melted but the WC is still solid. The furnace is evacuated to vacuum with a residual pressure of a few millibars depending on the degassing reactions taking place during heating [4]. The sintering atmosphere is of most relevance to reduce the compaction aid, to reduce the oxidation, and to avoid binder transport and surface decarburization during liquid sintering [1].

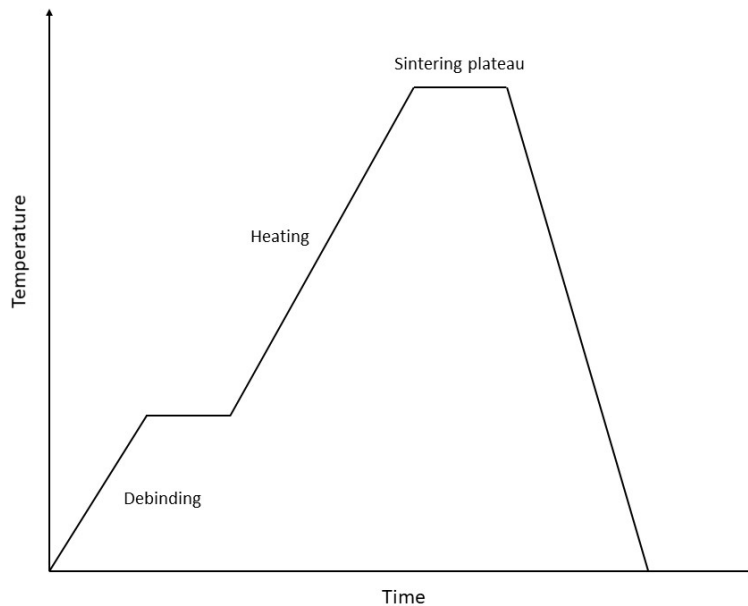


Figure 1: A schematic figure of the sintering cycle.

A part of the densification takes place already before the eutectic temperature of the pseudobinary WC-Co system is reached, i.e before the liquid phase sintering. However, the sintering

process is faster during the liquid phase sintering due to the enhanced atomic diffusion which enables material transport. The liquid phase sintering step could also be divided into three different stages; the initial stage, intermediate stage, and the final stage [7].

During the initial stage, rapid initial densification takes place soon after liquid formation due to the capillary force on the solid particles by the wetting liquid. Pore elimination takes place simultaneously since the system is striving to minimize the total surface energy. The maximum amount of densification achieved due to rearrangement of the particles is dependent on factors such as the amount of liquid present, solubility of solid in liquid, particle size, and contact angle. During the intermediate stage, the rearrangement of particles ends and the solution and reprecipitation process become dominant. The densification is related to grain shape adjustments, dissolution of small grains with reprecipitation on large grains, and coalescence. All these processes occur simultaneously at this stage of the liquid phase sintering [7].

The final stage is an extension of the sintering and reprecipitation process taking place during the intermediate stage. For most WC-Co systems, full densification is achieved before the final stage and further holding at this sintering temperature does not lead to any further densification. Furthermore, the final stage is important for microstructural evolution such as the size, shape and distribution of the grains, and distribution of the binder phase. These microstructural changes influence both magnetic properties and mechanical properties. Since the coarsening process is dominant during the final stage, an increase of the sintering time results in an increase in mean grain size and mean separation between the grains. The WC grain size distribution is however mainly determined by the milling condition [7]. Cemented carbides obtain nearly full density during sintering and the remaining porosity is negligible in most applications [4].

The solubility of WC in solid Co is important to keep in mind since it increases with temperature and is high at the temperature where the first liquid forms. During sintering, WC reacts with the binder where W and carbon (C) diffuse in the binder phase. This reaction proceeds until all concentration gradients reach equilibrium and the binder composition becomes homogeneous [8]. Control of the C content is also crucial in order to prevent unfavourable phases that impair the mechanical properties [1].

### 2.2 Microstructure

The sintering is one of the most important process steps affecting the microstructure and mechanical properties of cemented carbides [1]. During cooling, the Co will solidify into fcc-Co and sometimes hcp-Co. WC has a highly anisotropic structure, and therefore develops anisotropic crystal shapes during grain growth. The shape of the carbide grains can be described as a flat, triangular prism with truncated edges [7]. The main phases present in cemented carbides are hexagonal WC phase, Co binder phase and sometimes cubic carbide phases. The carbides are surrounded by the Co binder phase. Cemented carbide is a unique material in many ways. One unique feature is that the matrix phase (the Co binder) is the minority phase. A typical microstructure of a cemented carbide is shown in Figure 2, where the light grey prisms are WC grains surrounded by the dark Co binder phase.

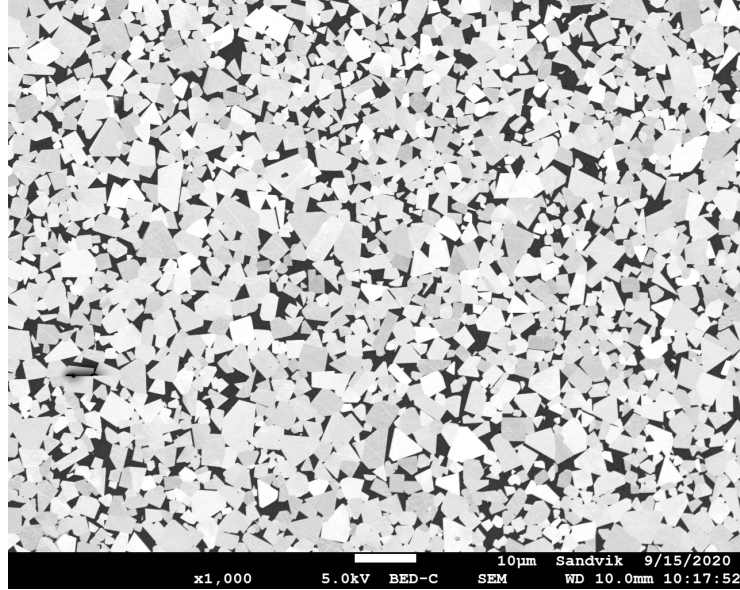


Figure 2: *Micrograph of a sintered two-phased WC-Co cemented carbide.*

The interaction between the binder phase and the carbides is what determines the final microstructure. There are several different quantities that can be used to describe the microstructure, e.g. WC grain size, contiguity, volume fraction of binder and the mean free path of the binder. However, it is usually sufficient only to state two of them to yield a good description of the microstructure. By adjusting the Co content and the size of the WC grains, the mechanical properties can be optimized for a specific application. Toughness, hardness and thermal conductivity are all dependent on these microstructural factors.

The C content is also a crucial parameter when producing cemented carbides since the so-called "carbon window", i.e the two-phase region of WC and fcc-Co, is very small. This can be seen in Figure 3. A higher C content will result in precipitation of graphite and a lower C content will result in precipitation of the  $\eta$ -phase ( $M_6C$ ). The graphite tends to worsen the mechanical properties, and the  $\eta$ -phase tends to decrease the toughness of cemented carbides. If the C content resides within the carbon window, all the melt will solidify before the composition reaches the ternary eutectic [1], [4].

## 2 CEMENTED CARBIDE

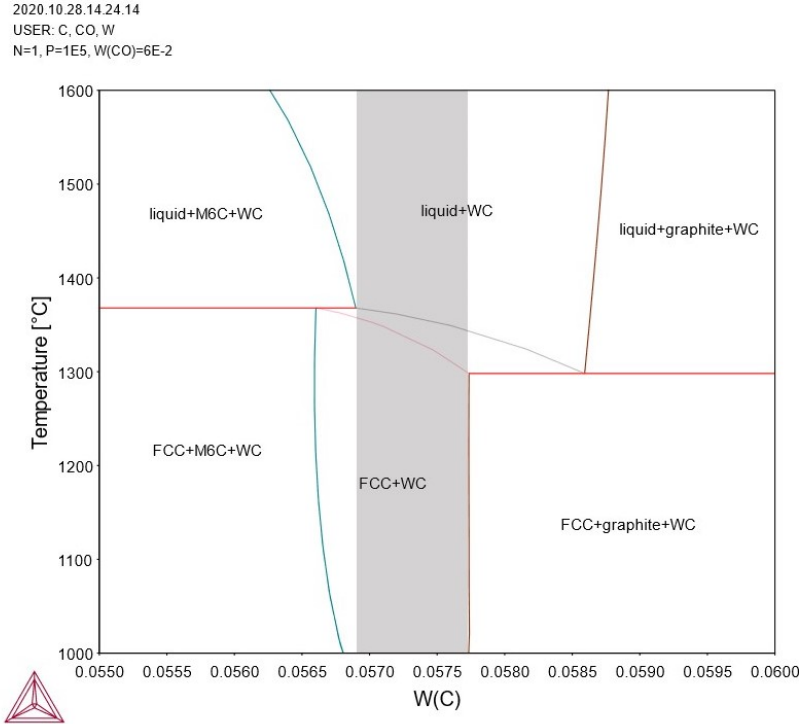


Figure 3: Vertical isopleth section of WC-6%Co system calculated with Thermo-Calc. The grey area represents the carbon window.

The solubility of W in the liquid Co phase decreases with increasing C activity, which is another reason for the importance of controlling the C content [1]. Varying the C content within the two-phase region can also influence the alloy properties. C contents near the upper limit result in high bending strength, low hardness and low coercive force. Hence, C contents near the lower limit results in low bending strength, high hardness and high coercive force [8].

### 2.2.1 Grain Size

The mechanical properties of cemented carbides mainly depend on composition and microstructure, most importantly the WC grain size. The control of the grain size is, therefore, a very important aspect and very useful for the quality control [9], [10]. Hardness and wear resistance generally increases with decreasing WC grain size. Since the metallic binder is softer and has higher toughness than the WC grains, an increase in volume fraction of the binder and WC grain size increases the fracture toughness but decreases the hardness and wear resistance [9].

The main mechanism of the growth of WC grains includes both diffusion during the solid sintering and dissolution and precipitation of WC in the Co-phase during the liquid phase sintering. Temperature and time are the two most important, and effective factors for controlling the grain growth during sintering. At the same holding time but with increasing temperature, the growth rate increases [11]. The growth behaviour of WC grains in cemented carbides is connected to both liquid content, and the liquid holding time [8].



When talking about the grain size of cemented carbides, it is often referred to as the WC grain size. The Co grains are much larger than the WC grains. The binder grain size is also an important aspect, but there are not many studies about the Co grain size. One study of Weidow and Andrén [12] showed that the Co grain size depends on many factors such as the composition of the binder phase, the cooling rate during sintering, the WC grain size, and the amount of binder phase.

### 2.2.2 Contiguity

The contiguity of cemented carbides is defined as the degree of contact between individual carbide grains [13], [14]. Contiguity is an important property of cemented carbides. It varies mainly with Co content and sintering time and gives insight into the sintering mechanism [1], [14]. The contiguity decreases with increasing binder content and also with increasing sintering time. The sintering temperature could also affect the contiguity, but not as significantly as the factors previously mentioned. It has been observed that an increase in temperature results in a decrease in contiguity [14].

Whether the contiguity is affected by the grain size or not is an ongoing discussion. Some researchers [15] claim that the contiguity is independent of the grain size, while others [16] claim that it is not independent and have derived expressions where the contiguity is a function of the grain size. However, Roebuck and Mingard [17] performed a study that compared and analyzed different contiguity models, where they concluded that there could be a grain size effect but that it is very small. They claim that the variation observed when calculating the contiguity with the different model expressions could be explained by aspects of the measurement technique rather than due to the grain size effect.

Considering contiguity and sintering parameters, it has been shown that the contiguity reaches an equilibrium value after a certain time. Warren and Waldron [18] showed that the contiguity is quite constant when varying the sintering time, but a study of Stjernberg [19] showed a slight increase in contiguity at very short sintering times. After prolonged sintering when the maximum contiguity was reached, the value decreased down to a constant value.

## 3 Characterization of Cemented Carbides

### 3.1 Hardness

Hardness can be defined as the resistance of a body to the penetration of another body [20]. The hardness of cemented carbides can be measured by different methods, such as Vickers, Rockwell, or Brinell hardness test. The hardness of a material is highly dependent on the material structure, especially the atom structure and the bonding force between the atoms. It is also related to different electric and magnetic properties [21].

The properties of WC-Co cemented carbides are very dependent on the WC grain size. The Hall-Petch relation fits well with both hardness and abrasion resistance, however, this may not be applicable for cemented carbides with a wide range of grain sizes. More research about models that relate grain size distributions with properties needs to be carried out [22]. A study of Cao et al. [10] shows that hardness and coercivity are inversely proportional to the content of coarse WC grains. This means that the influence a grain has on the macroscopic properties is proportional to its volume [10].

### 3.2 Magnetic Measurements

The use of non-destructive methods for characterization of cemented carbide is of high importance, since it is a very strong material and it can therefore be difficult to perform mechanical testing on this material which is also more time-consuming. Magnetic measurements can be performed on cemented carbides since they contain Co which has ferromagnetic properties. Therefore, measurements of magnetic properties are widely used in the cemented carbide industry. Both measurements of magnetic saturation and coercive force are used for this purpose and can be linked to the Co composition and thus overall properties and performance [23]. It is also possible to determine if the final product lies within the carbon window that ensures the most suitable properties of cemented carbides [1].

#### 3.2.1 Coercivity

Magnetic coercivity ( $H_c$ ) provides a characterization tool that indirectly measures the WC grain size. Cemented carbides with fine WC grain size have become more common and it is therefore important to be able to evaluate how the fine grain size affects the properties [24]. The composition of WC-Co cemented carbides is conventionally described in terms of the amount of Co and a nominal figure for the WC grain size. However, there is no widely agreed non-destructive method for WC grain size determination even though coercivity is the method most often used empirically [25].

Coercivity measures the electrical force needed to demagnetize a material after full magnetization. The electrical force required is mainly related to the Co/WC interphase area due to that the magnetic domain walls are pinned by these phase boundaries. The interphase area is therefore inversely related to the WC grain size. A fine microstructure (i.e. finer WC grains) results in higher interphase area which consequently results in higher coercivity [25], [26]. The coercive

forces of cemented carbides usually varies between 5-30 kA/m [27]. The measurement of coercivity is, however, independent of sample size and weight [26]

There are several factors that may affect the coercivity. The Co in the cemented carbides will alloy with the C or the WC during sintering, which will affect the coercivity. Changes in the Co composition will also have an effect which is important to take into account in empirical equations relating coercivity and WC grain size. However, the effect of cooling rate during sintering may result in changes in the composition of the binder phase which may cause difficulties when trying to relate coercivity with grain size. For example, precipitates of  $C_3W$  may form in the binder phase of cemented carbides with very low carbon content which will have a significant effect on the coercivity. Furthermore, phase boundaries between the fcc and the hcp phases within the binder regions may also affect the coercivity. Deformed cemented carbides also show a significant increase in coercivity due to the deformation that leads to creation of phase boundaries, stacking faults and mechanical twins.

It has also been shown that two materials with the same grain size but different contiguity will have different interphase areas, and therefore also different coercivity [25]. A study of Cao et al. [10] shows that the coercivity is inversely proportional to the grain size. Roebuck [24] has found the same relationship for cemented carbides with both 6wt% and 10wt% Co. Furthermore, the coercivity increases with decreasing Co-binder fraction [25].

#### 3.2.2 Cobalt Magnetic Saturation

Cobalt magnetic saturation (Co-m) is an indirect measurement of the carbon content of the binder. The term magnetic saturation refers to the maximum value of magnetic induction that can be obtained in a specimen in a strong magnetic field. The Co-m value gives information related to the composition of the binder phase. Information about the chemical composition, for example the amount of Co, is needed for proper analysis. The Co-m value can be expressed in several ways: as magnetic saturation of the cemented carbide or the binder phase, as the magnetic moment of the cemented carbide or the binder phase, or as percentage of the value that would be obtained for a pure Co binder [23].

During sintering, both C and W will dissolve in the Co binder-phase. The amount of dissolved W has a linear relation to the magnetic saturation of Co and is not affected by the amount of carbon in solution. Less dissolved W will lead to increased magnetic saturation (higher Co-m). There is a linear relation between the carbon content and the values of the magnetic saturation. The magnetic saturation increases as the amount of W in solid solution in the Co phase decreases and vice versa [1], [8]. The amount of W in the fcc-Co can therefore be calculated with following equation

$$\frac{Co - m[\%]}{Co[wt\%]} = \frac{(1 - x(fcc, W))100}{63} \quad (1)$$

where  $x(fcc, W)$  is mole fraction of W in fcc-Co. Co-m/Co can also be used as an indication whether  $\eta$ -phase or graphite is present or not. A value higher than 0.98 is an indication of graphite and 0.75 is an indication of  $\eta$ -phase [28].

### 3.3 Microscopy

#### 3.3.1 Light Optical Microscopy

Light Optical Microscopy (LOM) have been used widely by metallurgists to investigate the microstructure of materials since the 1880's [29]. LOM is also an important tool for quality control of cemented carbides. It is very useful for studying the overall microstructure but not for fine characteristics [30]. The image of the sample is formed by an objective lens, the magnified image is then viewed through an ocular. The magnification of the objective lens is usually in the range of 10x to 100x and the magnification of the ocular is commonly 10x. The total magnification is yielded by multiplying these two magnifications. The total magnification of LOM images is usually between 100x and 1000x. Most modern microscopes use the so-called infinite tube length approach where the objective forms an image of the sample at infinite distance [31].

#### 3.3.2 Scanning Electron Microscopy

The Scanning Electron Microscope (SEM) creates magnified pictures that reveal microscopic-scale information about the crystallography, composition, shape, size and other physical and chemical properties of the sample. SEM is most often used to study the surface and near-surface of bulk material. The basic operating principle involves a finely focused electron beam generated by emissions from an electron source [32]. The electrons are commonly generated by tungsten filament thermionic emission but for higher resolution, a field emission gun (FEG) is used [33]. The electron beam is scanned over the sample and at each of the discrete locations of the scan pattern, the electron beam interacts with the sample surface and two different outgoing electron products are produced: backscattered electrons and secondary electrons. These outgoing electrons are then measured by electron detectors [32]. The secondary electrons originate from the near-surface regions and are therefore commonly used for inspection of the topography of the surface of a sample. Backscattered electron imaging is often used for the inspection of compositional variations since the size of the atoms determines the signal of the backscattered electrons resulting in different contrasts in the image. Larger atoms create a higher signal and will therefore appear brighter in the image [33].

#### 3.3.3 Electron Backscatter Diffraction

Electron backscatter diffraction (EBSD) analysis is used to analyze the crystal structure of materials by a so-called diffraction pattern. The specimen must have a strain-free surface that is tilted to an angle of  $70^\circ$ . The diffraction pattern is formed on a transmission phosphor screen and recorded by a sensitive video camera that focuses on the other side of the phosphor screen. The diffraction pattern is analyzed with a PC and gives information about the crystal structure. The analysis program measures the angle between the lines of the diffraction pattern and their position and compares the result with the ones predicted for the crystal structure. The crystallographic orientation is then calculated and the pattern is stored. A SEM with a field emission gun (FEGSEM) can be used for improved resolution [33].

Both the resolution and the size of each map pixel of the EBSD measurement is determined by the step size chosen. Therefore, a step size as coarse as possible that still gives accurate data

is desired. It is also highly important that the sample has a flat surface that is highly polished and deformation free to get good diffraction patterns [22], therefore both mechanical and ion polishing is needed.

Zero solutions, i.e. non-indexed pixels will occur in the EBSD analysis due to the sample preparation (shadowed Co-phase) but also in WC/WC grain boundaries. However, zero solutions may be repaired by enlarging existing grains where they have a minimum number of indexed neighbours [22]. Today, this can be done as an automatic procedure in the EBSD software.

#### **3.3.4 Energy-Dispersive X-ray Spectroscopy**

Energy-Dispersive X-ray Spectroscopy (EDS) is a technique used together with an SEM that enable microanalysis of the chemical composition of a sample. It provides analyze of near-surface elements and their amount at different positions. The EDS technique depends on the ionization of the atoms in the sample. The energy loss of the ionization results in the emission of an element-specific X-ray which therefore can be used for chemical analysis by an energy dispersive detector. Since every element has a unique atomic structure, each detected element will have a unique set of peaks in the X-ray emission spectrum. The height of the peak indicates the fraction of that element at the specific position of the sample [34], [35].

### **3.4 Grain Size Determination**

The conventional way of measuring the grain size of cemented carbides is by the linear intercept method and equivalent circle diameter method by using SEM images. The principle of the linear intercept method is to measure the length of random intercepts and the equivalent circle diameter method is based on measuring the area of individual WC grains and calculating the diameter of a circle with an area equal to the area of the grain. These methods are often performed together with an image analysis software to make the measurements easier, but the problem with this method is that it can be hard to distinguish the WC/WC grain boundaries. However, when using these methods one could keep in mind that the grain size is three-dimensional, while the linear intercept method measures in one-dimension and the equivalent circle diameter method measures in two-dimension [10].

The arithmetic number average is generally used as the parameter when characterizing WC grain size. According to a study made by Cao et al. the cumulative distribution diameter D50 showed better correlation with the physical properties than the arithmetic number average [10]. The linear intercept method has been studied extensively by many researchers which has resulted in an international standard for grain size measurements that aims to ensure comparable and repeatable measurements. This method requires lengthy manual measurements and subjective interpretation of the grain boundary position which can be affected by the level of etching and change in contrast [22].

The EBSD technique can be used for grain size determination. As previously described, EBSD is a SEM method that steps the electron beam across the sample and determines phase and crystallographic orientation of the sample at each step. The maps produced of the microstructure can

easily be analyzed by using the crystallographic information to determine the size and relative location of the phases, grains, and grain boundaries. It is relatively quick to achieve different analysis parameters once the sample is mapped. The mean value calculated from an EBSD map will be highly affected by the number of small grains. The number of small grains measured is dependent on both the step size and the level of noise. The size of the smallest grain is defined to reduce the effect of the noise. However, the effect of the small grains can be reduced significantly by using averages based on area [22].

### 3.5 Contiguity Determination

Usually, the proportion of WC/WC grain boundaries is measured since the unique properties of cemented carbides are mainly due to the formation of the so called WC skeleton which is formed during sintering [1]. Contiguity can be determined in similar ways as grain size, by a line intercept technique in suitable micrographs. Contiguity is defined as the ratio of grain boundary surface to total surface, described in equation (2)

$$C_{WC} = \frac{2N_{WC/WC}}{2N_{WC/WC} + N_{WC/Co}} \quad (2)$$

where, in unit length of line,  $N_{WC/WC}$  is the number of carbide-carbide interfaces and  $N_{WC/Co}$  is the number of carbide-binder interfaces that are intercepted [13], [14]. At least 300 phase regions should be traversed before the measured contiguity converges sufficiently [36]. Researchers have studied the relationship between WC contiguity and the volume fraction of the binder and found expressions for this relation, shown in Table 1. By relating the properties of cemented carbides to the Co content and the average grain size a good description of the properties, such as hardness, can be achieved [1].

Table 1: *Expressions relating contiguity to the volume fraction of Co binder.*

Reference	Contiguity expression
Roebuck and Bennet [36]	$C_{WC} = 0.85 - 1.80V_{Co}$
Exner and Fischmeister [37]	$C_{WC} = 0.074V_{Co}^{-1}$
Stjernberg [19]	$C_{WC} = 1 - \sqrt{1 - V_{WC}^2}$

The EBSD technique has started to become more common for microstructural measurements, including contiguity. There are however no automatic routine for this today. Roebuck and Mingard [17] calculated the contiguity with the line intercept method and showed that the EBSD maps resulted in a contiguity value 15% higher than from SEM images. One explanation could be that the EBSD measurement has higher accuracy, but another explanation could be the artefacts during cleaning of raw data [17].

## 4 Method

### 4.1 Material and Sintering

Three commercial grades designated in this report as A, B and C were chosen. The relative Co content, WC grain size and addition of Cr of these materials can be seen in Table 2. All three powders were pressed into green bodies in the shape of drilling bit inserts and were thereafter sintered in a pilot-scale sintering furnace. The sintered samples had a diameter of 10 mm and a height of 16 mm after sintering. Holding time at maximum temperature and maximum sintering temperature were the same for all runs. The parameters that varied between the different sintering cycles were the cooling rate, and for the higher cooling rates, a pressure needed to be added to be able to control the cooling rate.

Table 2: *Relative amount of Co and WC grain size. Addition of Cr is indicated by yes (Y) or no (N).*

Material	wt% Co	WC grain size	Cr addition
A	-	-	N
B	+	+	N
C	+	+	Y

Sinterings with cooling rates between 14°C/min (free cooling) and 0.4°C/min down to 1000°C were carried out. The different cooling rates used together with the number of sintering cycles of each powder is presented in Table 3. Five green bodies of each powder were sintered each cycle. Most of the different sintering cycles were repeated to be able to detect any fluctuations of the properties of the sintered samples. However, powder C was not included at the start of this study and is therefore not included in all sintering batches, hence not sintered as many times. One sintering was performed with the production furnaces at SMRT to be able to compare how the properties varied between the different sintering furnaces. The exact cooling rate of that sintering was not possible to measure.

Table 3: *Number of sintering cycles for each powder and cooling rate.*

Cooling rate [°C/min]	Material A	Material B	Material C
14	2	2	2
8	2	2	2
5	2	2	2
2	2	2	1
1.4	1	1	1
0.8	3	3	2
0.4	3	3	2

## 4.2 Sample preparation

For the microscopy and the hardness test, one of the sintered inserts of each material and sintering cycle was cut in half and mounted in Bakelite-plastic. The mounted samples were ground and polished to achieve a flat surface without scratches and other irregularities. Before investigating the samples with LOM and SEM, etching in Murakami reagent for one minute was done to get more contrast between the phases to make it easier to distinguish the grain boundaries.

Before the EBSD analysis, the samples in the bakelite were cut into around 2.5 mm thin discs. To achieve plane parallel samples, the discs were ground on both sides and thereafter polished on the side to be examined. The cemented carbide was thereafter removed from the bakelite and cleaned in a ultrasonic cleaner. Ion polishing was then performed with the Hitachi IM-400 ion polisher for 90 minutes at 6V and for 20 minutes at 2V, both with an incident angle around 3°. The sample was then glued with epoxy onto a sample holder with an angle of 45° and painted with silver paint for improved conductivity.

## 4.3 Vickers Hardness

A Vickers Hardness test was performed manually on all the prepared samples with a Future-Tech FV-300 Vickers hardness tester and calculated with the JK LAB semiautomatic hardness measurement software version 5.118. Five indentations were made for each sample and the arithmetic mean was calculated. The indentations were placed along a line in the center of the sample. The indenter had a load of 20kg and the indentations were studied at 20x magnification.

## 4.4 Magnetic Measurements

Magnetic measurements were performed on the sintered cemented carbide inserts. Both cobalt magnetic saturation (Co-m) and magnetic coercivity (Hc) were measured. Both the Co-m measurements and the Hc measurements were performed with Foerster-Koerzimat 1.097 equipment.



An average of the magnetic properties was calculated for each powder of each sintering batch. The Hc values were also used for comparison with the hardness measurements.

### 4.5 Microscopy

The microstructure of all samples was studied with a ZEISS Axio Imager.A2m Light optical microscope. The aim was to detect any unwanted phases, such as  $\eta$ -phase or graphite, or other microstructural deviations that could affect the mechanical and magnetic properties. Three cooling rates of each material were chosen for the contiguity calculations which were performed on SEM images. This was also done for the production sintered samples. A JEOL 7800F FEGSEM were used with a backscatter electron detector with 15 kV acceleration voltage and 10mm working distance. The micrographs were taken with a magnification of both 1000x and 3000x.

### 4.6 Contiguity calculations

The contiguity was measured with the line intercept method on SEM micrographs and calculated with eq. (2). The contiguity calculations were performed on micrographs of three different sites of the sample with a magnification of 3000x. The line intercept method was carried out by hand on micrographs printed out on paper. Three different cooling rates were chosen for the contiguity calculations, 14°C, 5°C, and 0.4°C . Also, the production sintered samples were included in the contiguity calculations. The contiguity was also calculated by the binder volume fraction with the equations shown in Table 1. The volume fractions were calculated with Thermo-Calc at 1000°C since the composition is assumed not to change below this temperature [38].

### 4.7 Electron Backscatter Diffraction Analysis

The EBSD analysis was performed with a JEOL JSM-7800F FEGSEM with a NordlysMax2 EBSD detector using AZtec software version 3.4. The number of samples was limited to two cooling rates for the EBSD analysis, the fastest cooling rate (14°C/min) and the slowest cooling rate (0.4°C/min). The analysis was performed on all three materials at both cooling rates. Two maps, each with a size of 90x90 $\mu$ m, were performed in the bulk of the sample to get accurate representation of the sample. The aim was to get a map with less than 10% zero-solutions [39]. The settings for the EBSD analysis are shown in Table 4.

The post processing of the data was performed with the AZtecCrystal version 1.1. The data was cleaned with the auto clean function within the AZtecCrystal software including both noise reduction of zero solution pixels and wild spikes correction of incorrectly indexed pixels. To reduce the noise further, the definition of the smallest grain was set to 10 pixels for WC and 4 pixels for Co and  $Cr_7C_3$  and the critical misorientation angle was set to 3°, meaning that an angle larger than 3° between two different crystals are considered as grain boundaries [40]. The grain data were used for grain size distribution evaluation. However, incomplete grains along the edges of the map were removed from the data set used for these calculations. The Equivalent Circle Diameter (ECD) for the different Co-phases (i.e. fcc and hcp) and WC for all three materials, and the Cr-carbide for Material C, were also evaluated from the data.

Table 4: *Settings used for EBSD analysis*

<b>Instrumental Settings</b>	
Acceleration voltage [kV]	20
Aperature	2
Probe current	12
<b>Analysis Settings</b>	
Map area [ $\mu m^2$ ]	90x90
Number of maps	2
Step size [ $\mu m$ ]	0.1 & 0.07*
Binning mode	4x4
Index mode	optimize TKD
Number of bands	6
Included phases	WC, Co(fcc), Co(hcp), M7C3**

\*0.1 $\mu m$  used for Material B and C, 0.07 $\mu m$  used for Material A

\*\*M7C3 only included for Material C

The first EBSD analysis was not able to detect the whole Co grains due to the larger size. Also, there was a software limitation where the Co areas between the WC grains were counted as one grain. Therefore an additional analysis was made as an attempt to determine the whole Co grain size. For this analysis, the two samples of material A was studied with EBSD at lower magnification. The slow cooled sample had a map area of 170x180 $\mu m$  with a step size of 0.07 $\mu m$  and the fast cooled sample had a map area of 200x150 $\mu m$  with a step size of 0.1 $\mu m$ . Only one map of each sample was conducted. The post-processing parameters for these maps were the same as for the previous maps. Inverse pole figure (IPF) maps, where the grains are colored based on the measured orientation, in both x,y and z-direction were used for identifying the different fcc-Co grains, in a similar way as Weidow and Andr  n [12]. The grain boundaries were interpreted and marked manually. The line intercept method was used for calculating the average Co grain size. Since the hcp-Co was too small, it was excluded from these calculations.

#### 4.7.1 Grain Size Distribution Evaluation

The WC grain size distribution evaluation from the EBSD data was performed with Matlab using a code provided by Sandvik Coromant R&D which calculates both grain statistics and distribution [41]. The size distributions were presented with cumulative and frequency plots, using both area and number fraction on the y-axis and circle equivalence diameter on the x-axis. The Matlab program also calculated the number of grains, average diameter, standard deviation and the area based parameters D10, D50, D90, and D100. The area based parameter D50 is the equivalent

diameter where 50% the grains have a diameter smaller than this value. In the same way, 90% of the grains have a diameter smaller than  $D_{90}$ , and 10% have a diameter smaller than  $D_{10}$ . Hence,  $D_{100}$  describes the largest grain. The grain size distribution width (GSDW) was calculated with eq. (3) which gives a measurement of the width of the grain size distribution.

$$GSDW = \frac{D_{90} - D_{10}}{D_{50}} \quad (3)$$

The grain size distribution statistics from the EBSD is also presented with a Sandvik internal method developed at Sandvik Coromant [42]. This method presents the cumulative number of grains (in logarithmic scale) that is larger than the equivalent diameter. This way, the number of large grains is presented in a clearer way.

### 4.8 Thermodynamic Calculations

The thermodynamic software Thermo-Calc was used to create phase diagrams for the investigated materials. The database used was Sandvik's internal database [43] for cemented carbides. Thermo-Calc was also used to calculate both the liquidus and the solidus temperature at a specific carbon content. The carbon content and the amount of W in the fcc-Co phase ( $x(\text{fcc}, \text{W})$ ) were used as input for these calculations.  $x(\text{fcc}, \text{W})$  was calculated with eq. (1) which is described in section 3. The calculated values of the liquidus and solidus temperatures were then used, together with the trend data from the sintering furnace, to calculate for how long the binder phase has been totally melted (only liquid phase) and partly melted (liquid and fcc phase). This was only applicable to materials A and B since material C contains Cr and eq. 1 is therefore not valid for that material.

## 5 Results

### 5.1 Magnetic Properties and Hardness

The results for the magnetic properties are presented below. Each presented value in the figures indicates the average for each sintering cycle since all five samples of each material were measured. Since it was not possible to measure the cooling rate in the production furnace, it was estimated to  $0.6^{\circ}\text{C}/\text{min}$  based on the magnetic properties and the hardness values. The results of the Co-m measurements for all sintering cycles are shown in Figure 4. It can be seen that there is no significant variation of Co-m for the different cooling rates. Material C showed the largest variation in Co-m values overall. Co-m/Co was also calculated for all three materials. This resulted in a Co-m/Co value of around 0.93 for material A, 0.94 for material B, and 0.87 for material C which indicates that the composition lies within the carbon window, hence no graphite or  $\eta$ -phase should be present in any of the materials.

Figure 5 shows how the coercivity varies with different cooling rates for the three different materials. Material A was the material used in the previous studies at SMRT that showed a variation with the cooling rate. The same result was found in this study. A faster cooling rate yields higher coercivity values for material A. It can also be seen that the coercivity for material A is more affected by the cooling rate than material B and C. The coercivity values for Material B and C are almost constant compared to the variation for material A. The production sintered samples showed similar coercivity and Co-m values as for the samples sintered in the pilot-scale furnace.

## 5 RESULTS

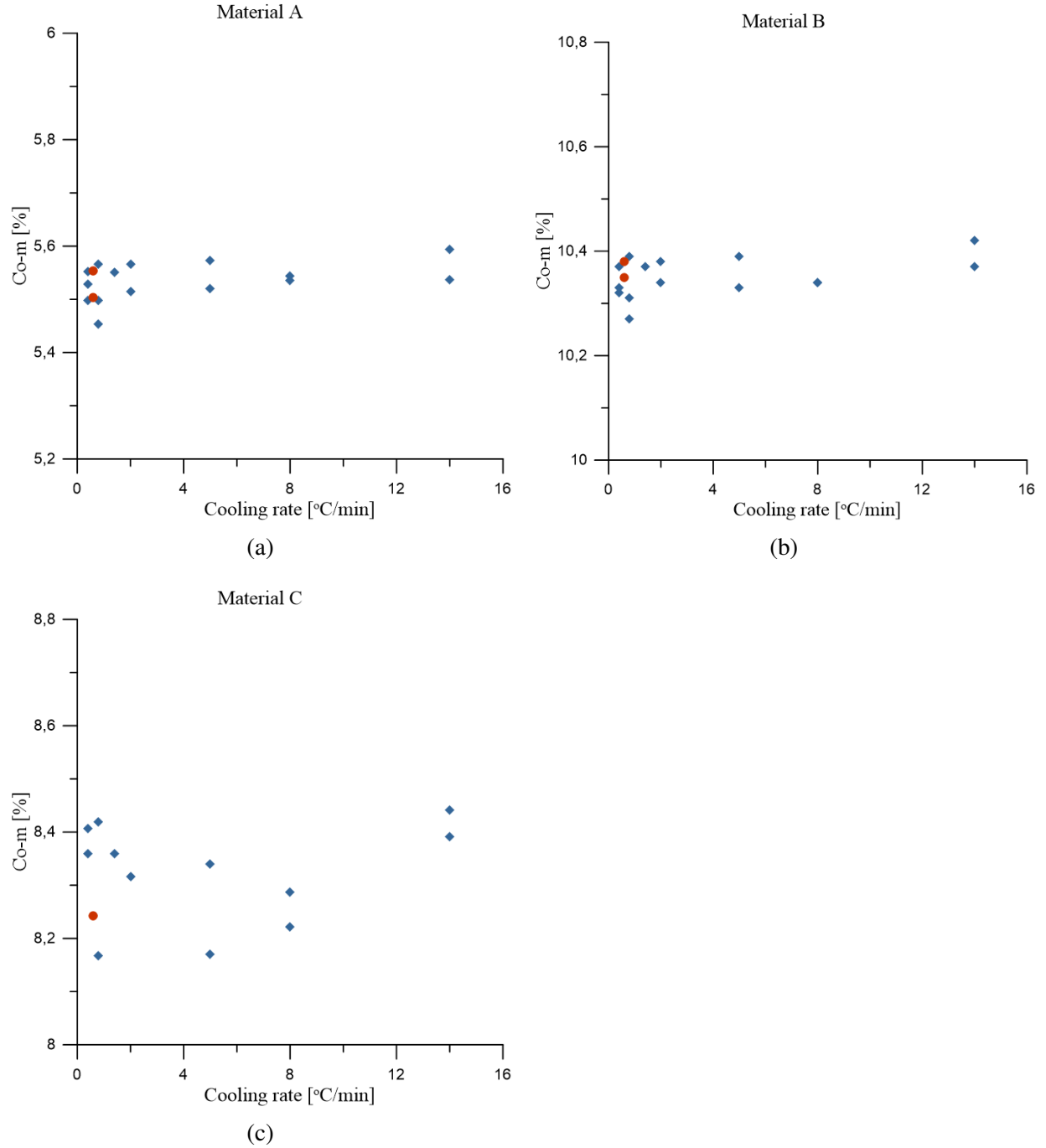


Figure 4: Measured Co-m at different cooling rates for (a) material A, (b) material B, (c) material C. The red dots indicate the Co-m value for the samples sintered in the production furnace. The standard deviation for these measurements were around 0.01-0.02.

## 5 RESULTS

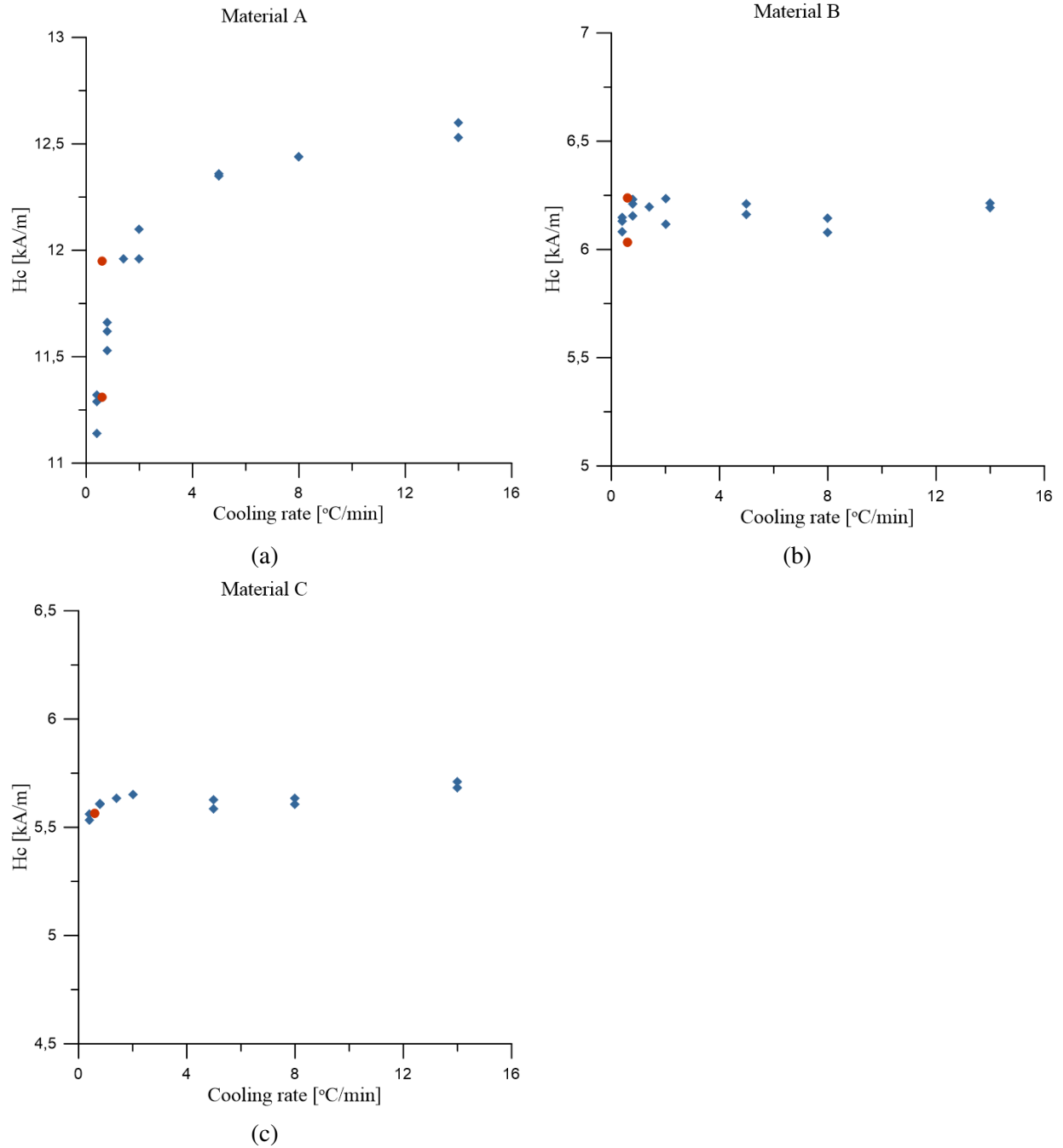


Figure 5: Measured coercivity ( $H_c$ ) at different cooling rates for (a) material A, (b) material B, (c) material C. The red dots indicate the  $H_c$  value for the samples sintered in the production furnace. The standard deviation for these measurements were around 0.01-0.03.

The measured coercivity was also compared to the Vickers hardness values for all three materials which are shown in Figures 6-8. For material A, there is a slight increase in hardness with an increased cooling rate and coercivity, as seen in Figure 6b. However, the differences are relatively small in comparison to the standard deviation for the hardness measurements that varied between 4-15 HV. This makes the increase less noteworthy. The hardness values of the production sintered

## 5 RESULTS

samples are similar to the samples sintered in the pilot-scale furnace.

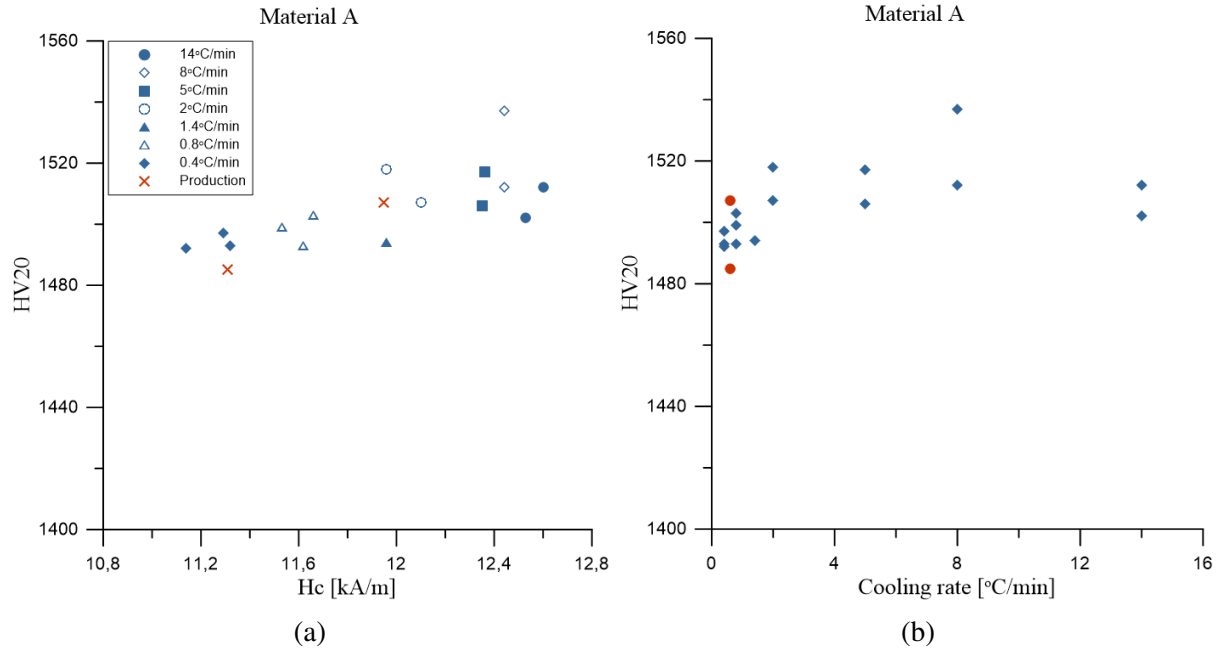


Figure 6: Vickers hardness values for material A compared to (a) coercivity ( $H_v$ ) and (b) cooling rate. The values for the production sintered samples are shown in red.

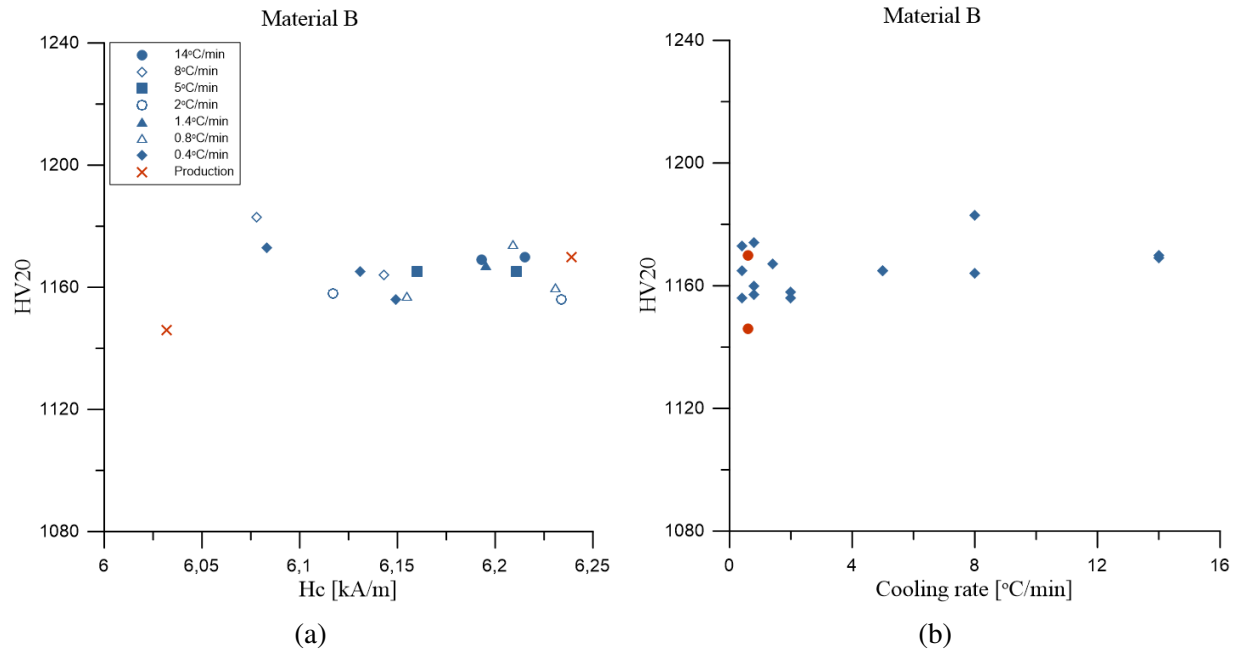


Figure 7: Vickers hardness values for material B compared to (a) coercivity ( $H_c$ ) and (b) cooling rate. The red values indicates the values for the production sintered samples.

## 5 RESULTS

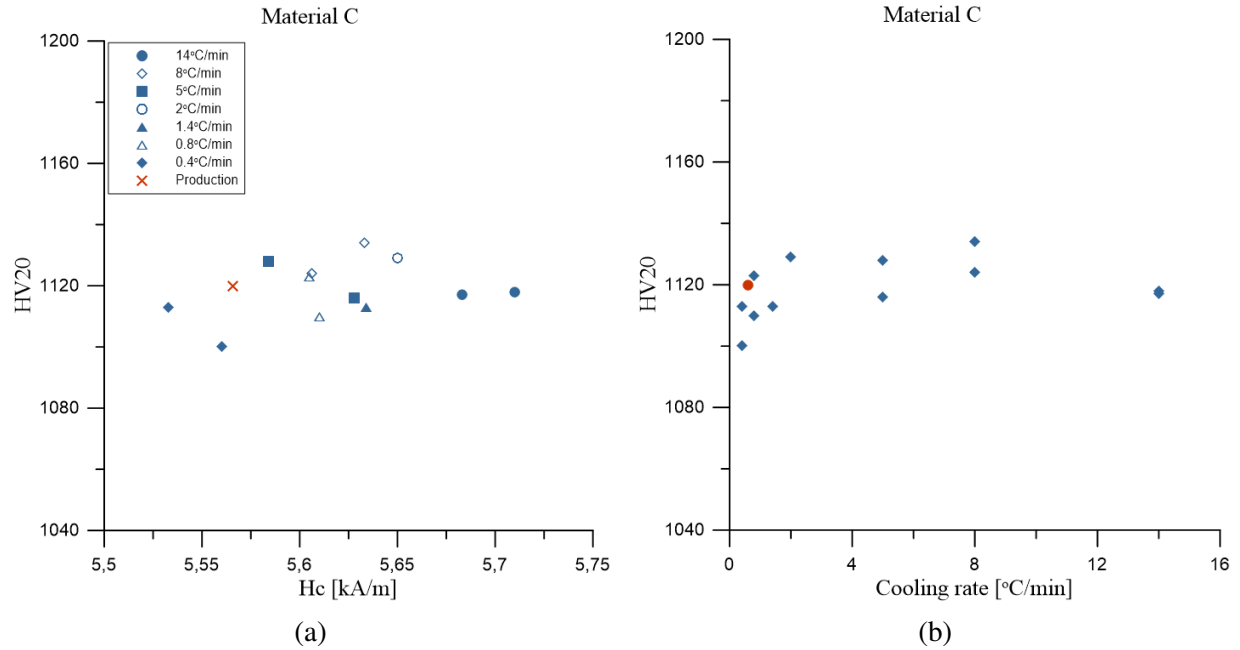


Figure 8: Vickers hardness values for material C compared to (a) coercivity ( $H_c$ ) and (b) cooling rate. The red values indicates the values for the production sintered samples.

## 5.2 Microstructure

### 5.2.1 Phase Observation

When studying the samples in LOM, an unknown phase similar to  $\eta$ -phase was found in the samples of materials A and B that were sintered in the pilot-scale sintering furnace. The phase was present for all different cooling rates for both materials A and B but was not present in either the production sintered samples or any sample of material C. The unknown phase present in material A can be seen in Figure 9. This result was not expected due to the high Co-m/Co values and was found late in the study. The fraction of this phase between materials A and B are similar. The EDS point analysis showed that the phase not only contained C, Co and W but also around 30at% Boron (B). It is important to note that the EDS method is not reliable for the exact composition of light elements, such as B, but can give an indication that these elements are present. The unknown phase is seen as black areas in Figure 9a and as light grey in Figure 9b.



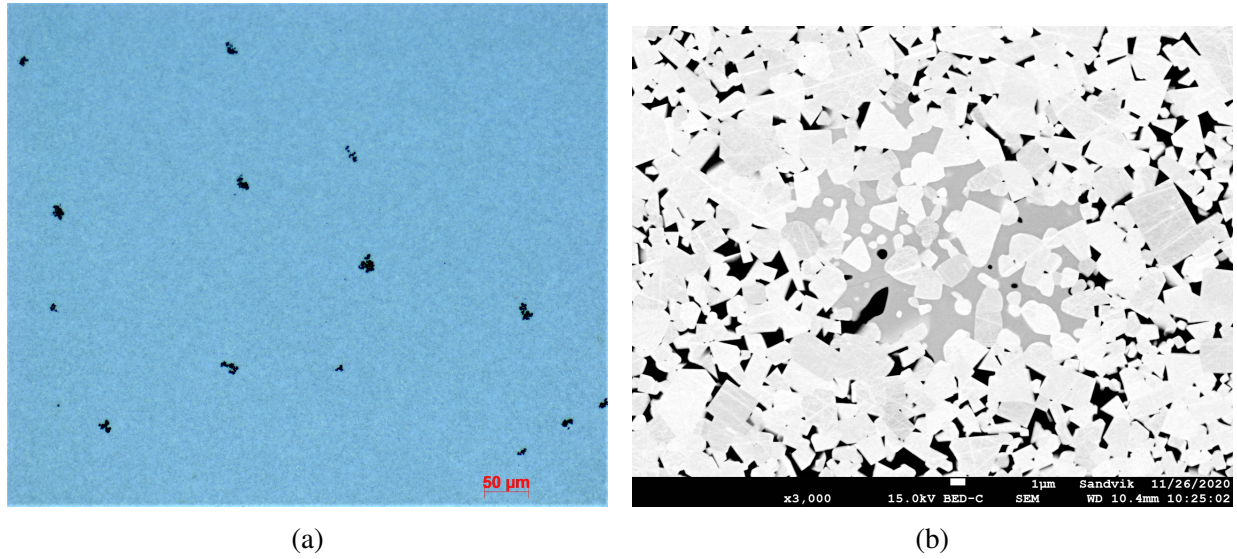


Figure 9: Micrographs from (a) LOM with x200 magnification and (b) SEM with x3000 magnification showing an unknown phase similar to the  $\eta$ -phase present in material A. In (a) the phase is seen as black areas and in (b) as grey areas between the white WC grains.

### 5.2.2 Grain Size Distribution

The grain size distribution for the WC grains from the EBSD analysis are shown in Figure 10. Surprisingly, the results show no significant variation of WC grain size between the different cooling rates for any of the materials, which could be expected at least for material A due to the coercivity variation. However, comparing the different materials it is clear that material C has the largest WC grain size and that material A has the smallest WC grain size as expected. D50 for WC grain size, as shown in Table 5, also indicates that the difference between the different cooling rates is negligible for all three materials. Material A also show a wider grain size distribution compared to the other materials.

Table 5: D50 for WC and the WC grain size distribution width for different cooling rates.

Material	WC		
	Cooling rate [°C/min]	D50 [ $\mu\text{m}$ ]	GSDW
A	0.4	1.86	1.33
	14	1.77	1.28
B	0.4	3.02	1.11
	14	3.13	1.03
C	0.4	4.52	1.16
	14	4.36	1.10

## 5 RESULTS

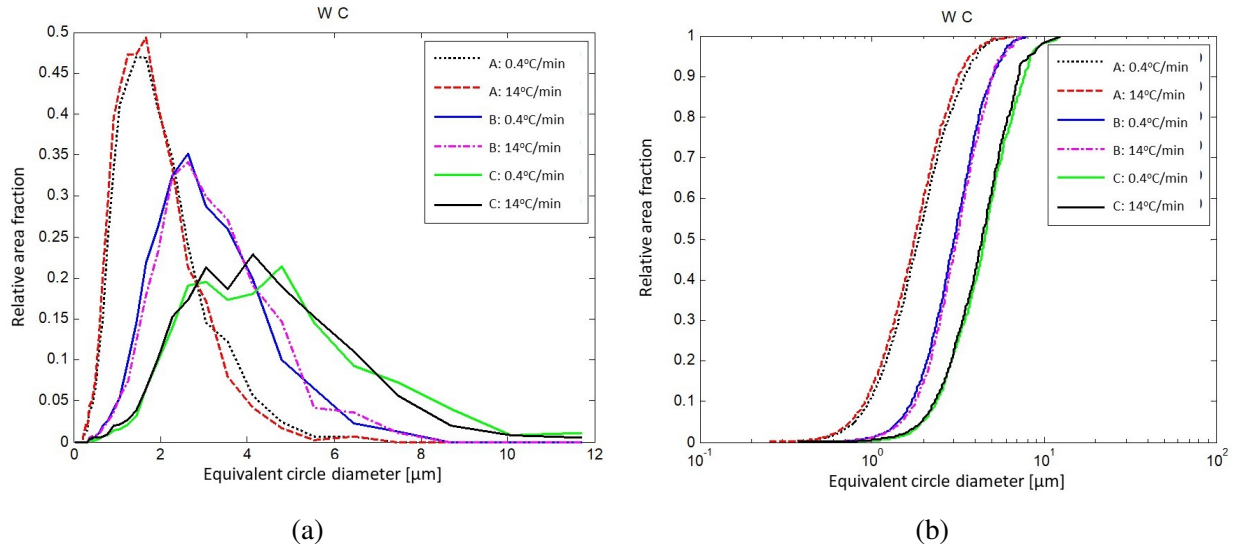


Figure 10: Area based WC grain size distribution for all three materials, both frequency (a) and cumulative (b) distributions.

The results from the Sandvik internal method for the WC grain size distribution presentation are presented in Figure 11. No significant difference between the different cooling rates was shown in these results. This indicates that the number of large grains between the different cooling rates does not differ significantly.

## 5 RESULTS

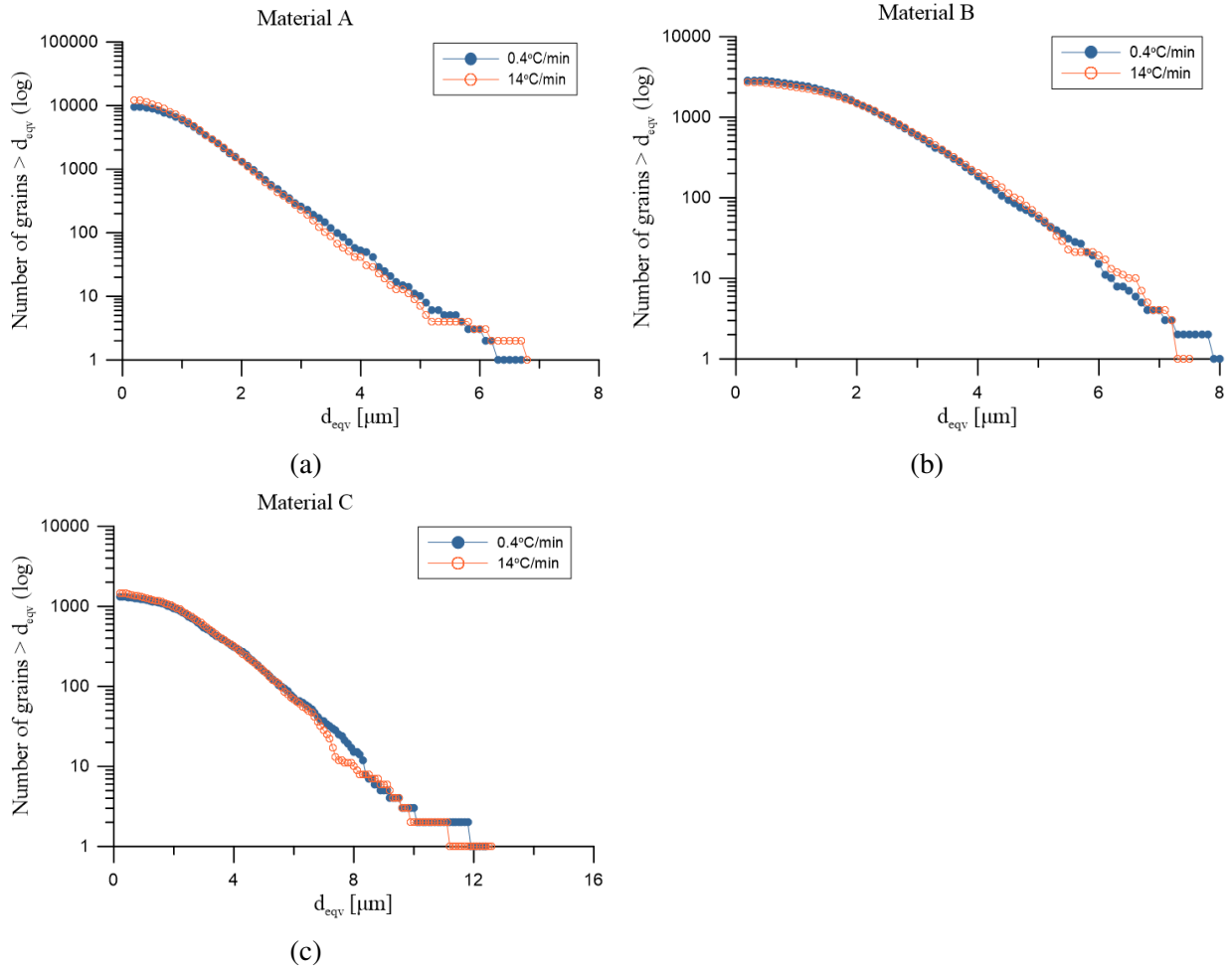


Figure 11: WC grain size distribution based on the Sandvik internal method for (a) material A, (b) material B, and (c) material C.

Due to limitations in the AZtec software, the statistics of the Co grain size distribution only showed values of the binder area between the different WC grains and not the whole binder grain. Figure 12 shows the size distribution of the Co areas between the WC grains of the different samples. For material A, this result showed that there are smaller binder areas between the WC grains for the fast cooled sample than for the slowly cooled sample. This difference was also seen on the IPF images of material A, shown in Figure 13. This results in a larger Co/WC interphase area. No significant difference in Co size between the different cooling rates was found for materials B and C.

## 5 RESULTS

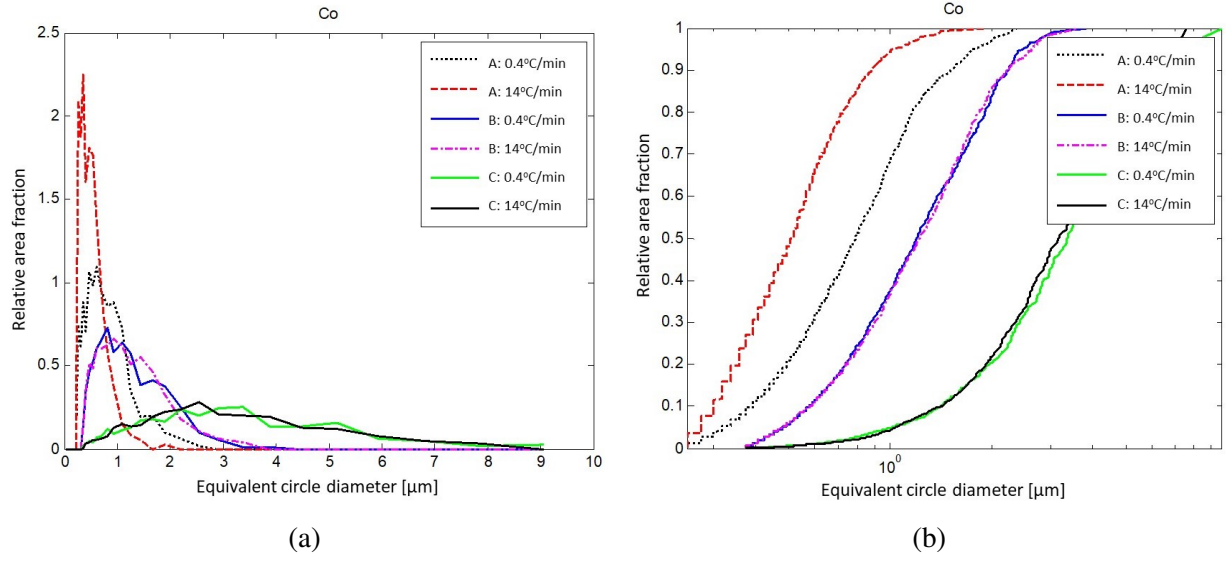


Figure 12: Area based size distribution of the Co areas between the WC grains for all three materials, both (a) frequency and (b) cumulative distributions.

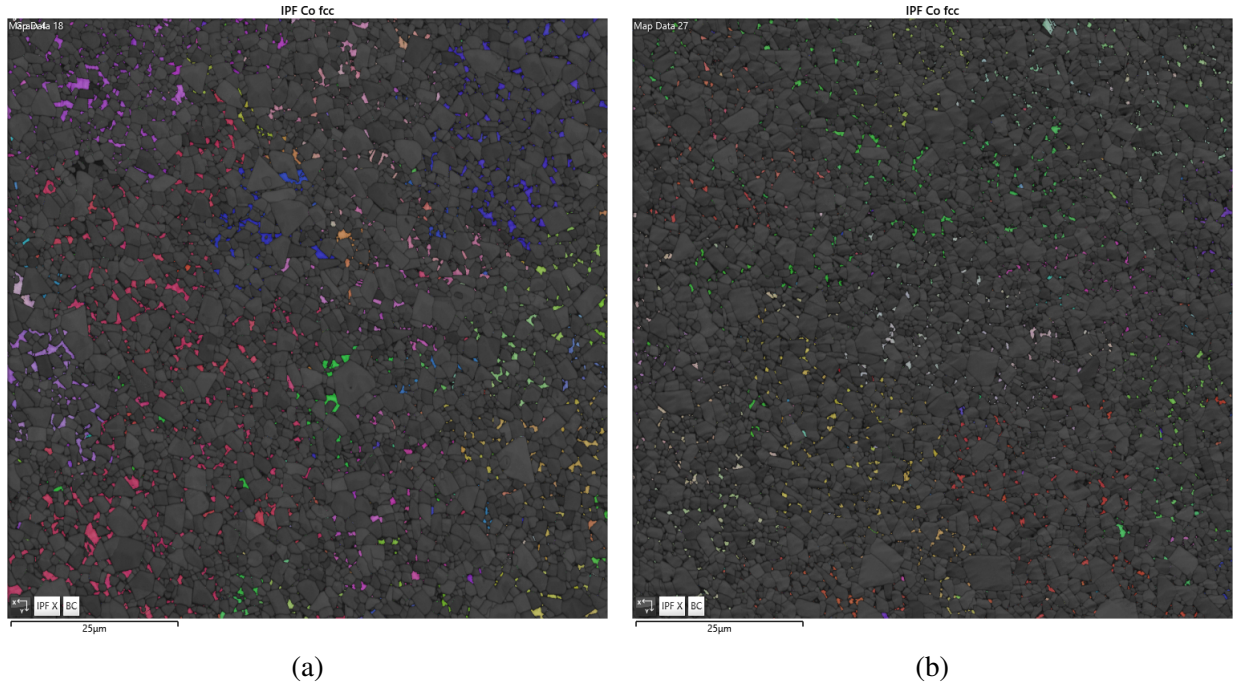


Figure 13: EBSD images of material A showing the fcc-Co grains for (a) 0.4°C/min and (b) 14°C/min. The different fcc-Co grains are indicated by different colors and the grey areas are WC grains.

In the EBSD analysis it was also found that both fcc-Co and hcp-Co were present in all materials. This can be seen in Figure 14. The two different Co-phases, fcc and hcp, were studied separately for material A where it was shown that the both the hcp and fcc grains were smaller in the fast

## 5 RESULTS

cooled sample, shown in Figure 15. The area fraction of the fcc-Co is significantly smaller for the fast cooled sample for material A, which is shown in Table 6. This confirms the differences shown in Figures 12 and 13. It is also shown that the area fraction of hcp-Co was much lower than of fcc-Co and that the hcp-grains are much smaller than the fcc grains. However, the area fraction of hcp-Co did show a slight increase for the fast cooled sample of material A, while the size of the hcp-Co grains decreased. This results in a larger interphase area between the hcp/fcc phases. The area fraction of hcp-Co did not differ as much as the area fraction of fcc-Co between the different cooling rates for material A. The change in area fraction of hcp-Co and fcc-Co for materials B and C were negligible.

Table 6: *Area fraction of hcp-Co and fcc-Co and D50 of the hcp-Co grains and fcc-Co areas for different cooling rates.*

Material	Co				
	Cooling rate [°C/min]	Area frac. fcc-Co [%]	Area frac. hcp-Co [%]	D50 fcc-Co [ $\mu m$ ]	D50 hcp-Co [ $\mu m$ ]
A	0.4	3.9	0.70	0.74	0.42
	14	1.6	0.85	0.42	0.32
B	0.4	9.4	3.4	1.3	0.73
	14	9.5	3.3	1.3	0.68
C	0.4	15	0.18	3.3	0.41
	14	15	0.15	3.0	0.30



## 5 RESULTS

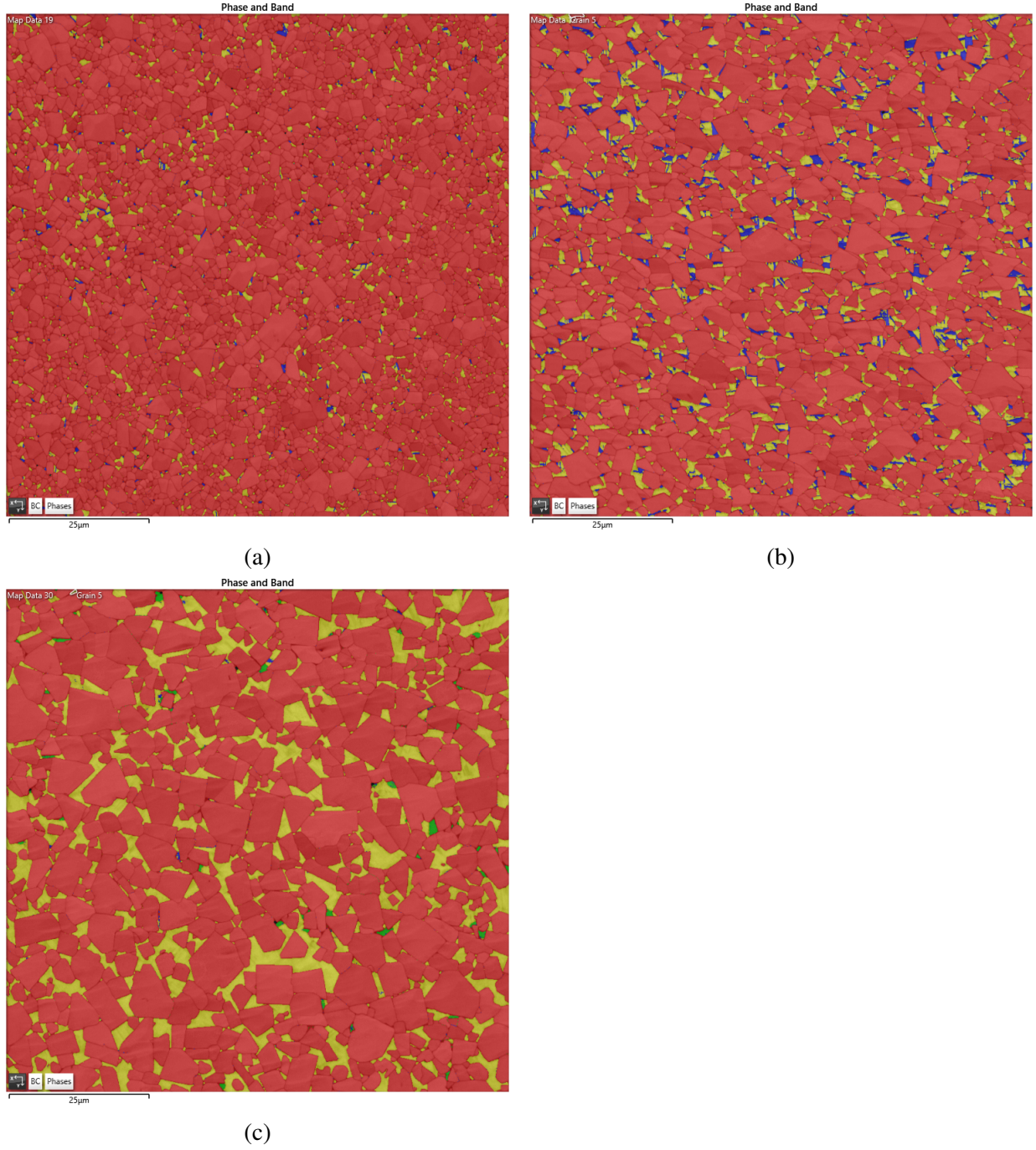


Figure 14: EBSD images of (a) material A and (b) material B and (c) material C, all with a cooling rate of  $0.4^{\circ}\text{C}/\text{min}$ . The red areas indicate WC, yellow indicates fcc-Co and blue indicated hcp-Co. For material C green indicates  $\text{Cr}_7\text{C}_3$ .

## 5 RESULTS

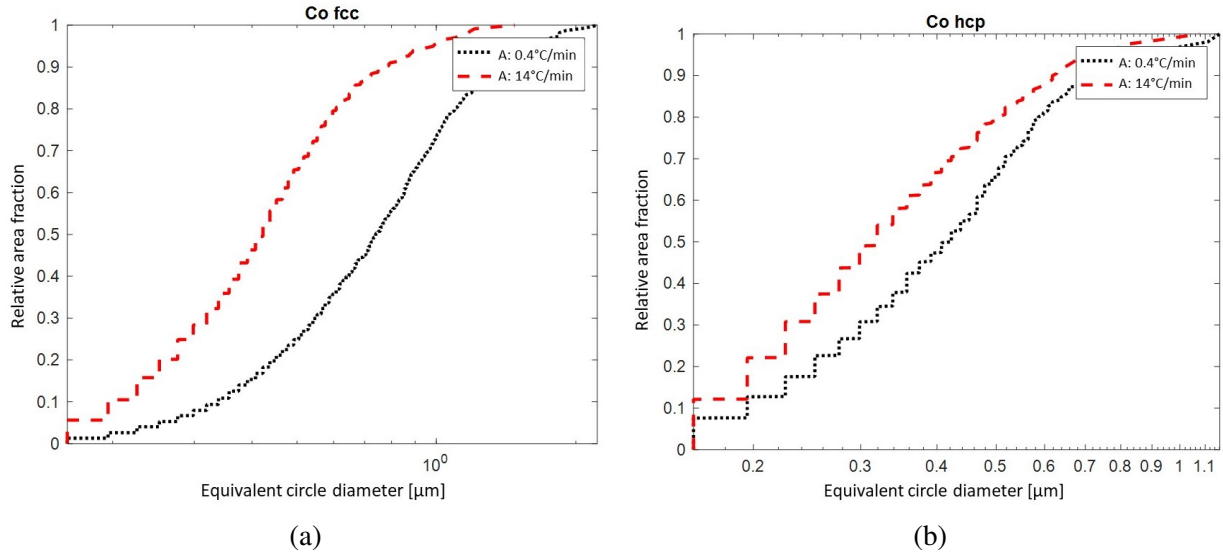


Figure 15: Cumulative area based size distribution for (a) the fcc-Co areas between the WC grains and (b) the hcp-Co grains for material A.

An attempt to measure the grain size of the whole Co binder grains was also made, to see if it was possible to detect any differences between the different cooling rates for material A. The different Co grains are indicated by different colours due to IPF coloring and the grain boundaries are marked with a black line by hand, shown in Figure 16. Due to limitations on the sample size of the EBSD technology in combination with the large grain size of the Co grains as well as time limitations, the number of measured Co grains for each sample was very small. Because of this, it was not possible to get a reliable estimate of the average Co grain size for the samples. Figure 16 also shows that small grains appear in some of the larger grains which indicates dendritic grain growth.

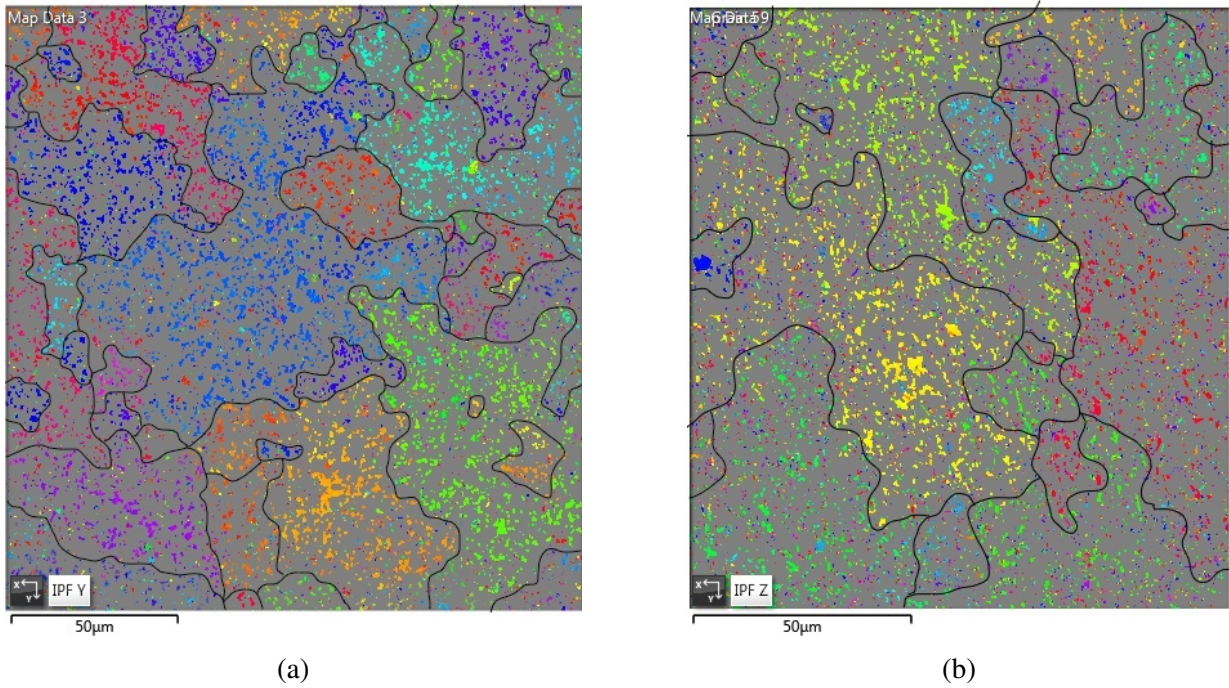


Figure 16: IPF image of material A where (a) shows the slow cooled sample and (b) the fast cooled sample. The different colors represent different fcc-Co binder grains, the grey areas are WC grains and the perceived Co grain boundaries are indicated by black lines.

Comparing the IPF images of material A and material B at the same cooling rate ( $0.4^{\circ}\text{C}/\text{min}$ ), it can be seen that material B has fewer and larger fcc-Co grains compared to material A. This can be seen in Figure 17. The map area for each of the two samples is  $90 \times 90 \mu\text{m}$ .



## 5 RESULTS

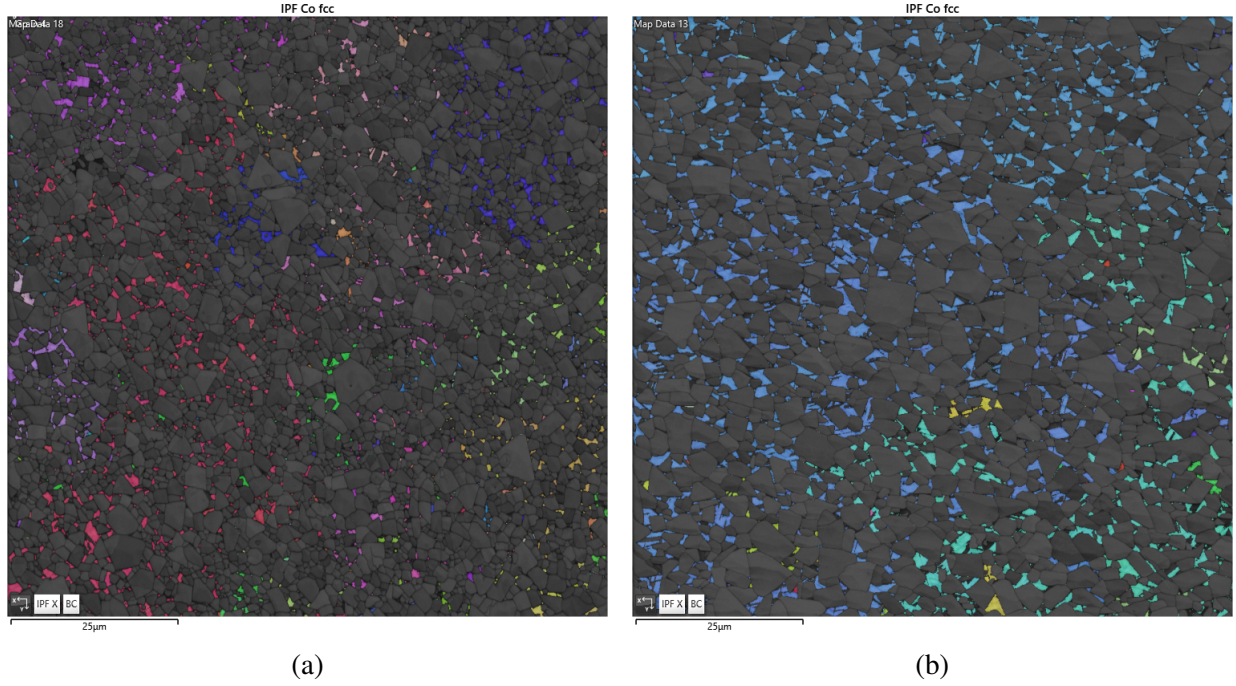


Figure 17: IPF image of (a) material A and (b) material B, both with a cooling rate of  $0.4^{\circ}\text{C}/\text{min}$ . The different colors represent different fcc-Co binder grains, the grey areas are WC grains.

For material C, which was the only material with Cr additions, the  $\text{Cr}_7\text{C}_3$  grain size distribution seems to differ between the different cooling rates. Figure 18 shows that the fast cooled sample ( $14^{\circ}\text{C}/\text{min}$ ) has finer grain size than the slow cooled sample ( $0.4^{\circ}\text{C}/\text{min}$ ). As seen in Table 7, the average grain size (D50) also indicate that the slowly cooled sample has larger  $\text{Cr}_7\text{C}_3$  grains. However, it is important to note that the number of  $\text{Cr}_7\text{C}_3$  grains are relatively few which may affect the statistics.

Table 7: Average  $\text{Cr}_7\text{C}_3$  grain size (D50) and grain size distribution width for different cooling rates.

Material	$\text{Cr}_7\text{C}_3$		
	Cooling rate [ $^{\circ}\text{C}/\text{min}$ ]	D50 [ $\mu\text{m}$ ]	GSDW
C	0.4	0.73	1.04
	14	0.48	0.83

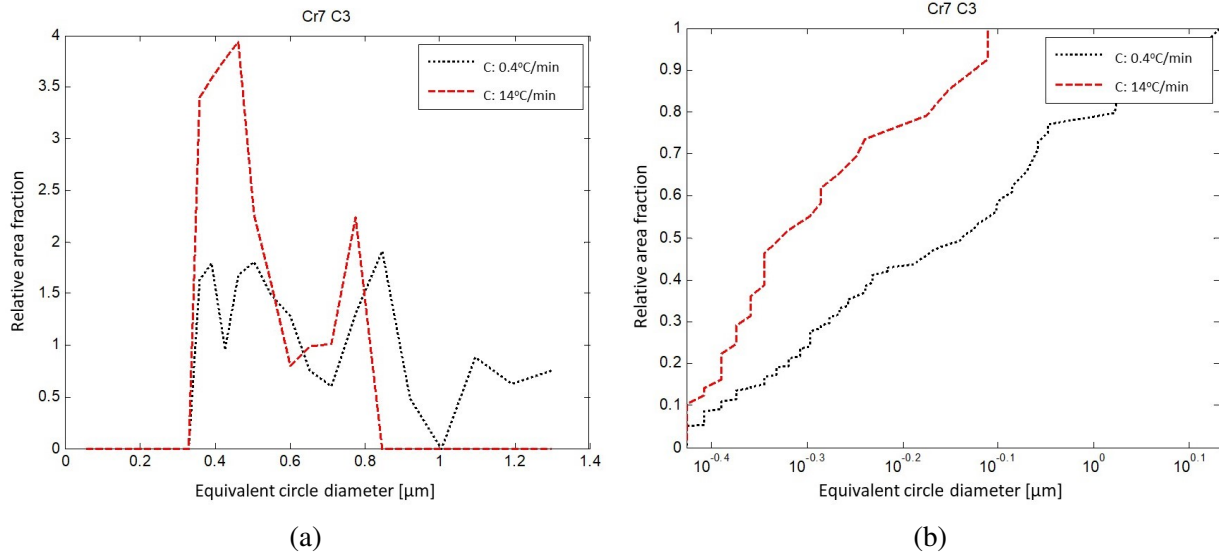


Figure 18: Area based  $Cr_7C_3$  grain size distribution for all three materials, both frequency (a) and cumulative (b) distributions.

### 5.2.3 Contiguity

The contiguity calculated with the line intercept method is shown in Figure 19. Material A has a higher contiguity than both material B and material C. There is a difference between materials B and C as well, but the standard deviation indicates that these measurements are ambiguous. However, the difference is not statistically significant for all cooling rates. The production sintered materials are in line with the other values, except for material C where the production sintered materials have a significantly higher value. The standard deviation of the production sintered sample for material C is 0.06 and the difference is therefore not statistically significant. The cooling rates for the production sintered samples were only an estimation based on the properties and could therefore be inaccurate.

Table 8 shows the contiguity calculated based on the binder volume fraction with the equations in Table 1 together with an average of the line intercept values. From the results in Table 8 it is shown that the contiguity values calculated based on the binder volume fraction are in line with the values calculated from the line intercept method.

Table 8: *Contiguity values calculated with different equations.*

Reference	Material A	Material B	Material C
Roebuck and Bennet [36]	0.66	0.51	0.47
Exner and Fischmeister [37]	0.68	0.39	0.35
Stjernberg [19]	0.55	0.41	0.38
Line intercept	0.66	0.50	0.39

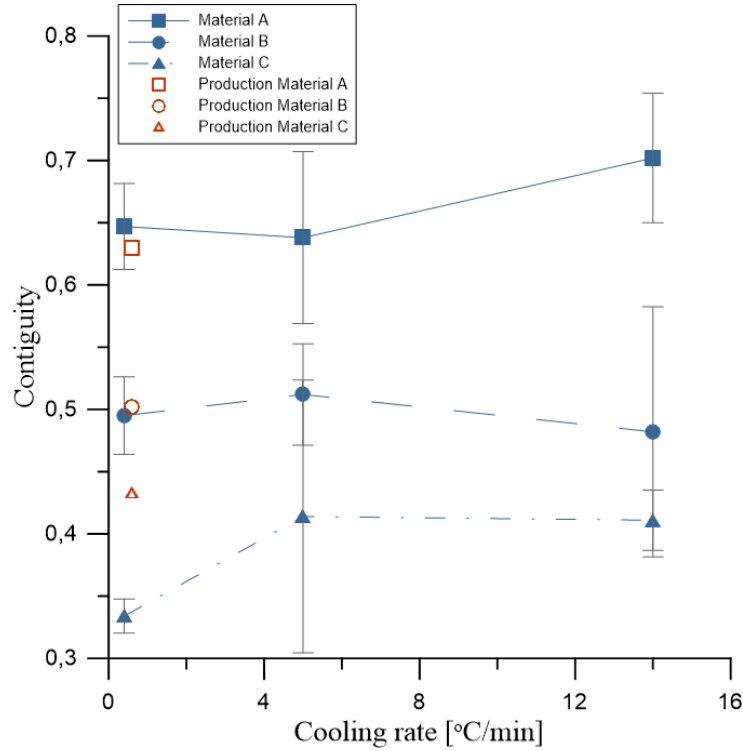


Figure 19: *The contiguity for the three different materials at three different cooling rates. The red dot indicates the contiguity for the production sintered samples. The error bars shows two standard deviations.*

### 5.3 Thermodynamic Calculations

The thermodynamic calculations together with the  $x(\text{W, fcc})$ -value, calculated from the Co-m values, showed that there is a significant difference in time at liquid state for the different cooling rates, as shown in Table 9. It shows the time in the three-phase region where solid WC, solid fcc-Co and liquid Co are present (time in WC+fcc-Co+liq) and the time in the two-phase region where only solid WC and liquid Co are present (time in liq+WC). The difference in time in the two-phase region (liquid and WC) between the slowest cooling rate and the fastest cooling rate is

## 5 RESULTS

---

114 minutes for material A and 121 minutes for material B. The difference in time over solidus temperature is even larger, 151 minutes for material A, and 170 minutes for material B.

Table 9: *Calculated values of time in liquid state, both time over solidus temperature and over liquidus temperature.*

Material	Cooling rate [°C/min]	Time over solidus temp. [min]	Time over liquidus temp. [min]
A	14	145	140
	5	155	149
	0.4	296	254
B	14	148	142
	5	159	150
	0.4	318	263

## 6 Discussion

The main aim of this study was to investigate why the coercivity changes with different cooling rates during sintering. As the results show, the coercivity of material A is notably affected by the cooling rate of the sintering. As the literature study shows, there could be several explanations for this behaviour. The same behaviour could be expected for all three different materials, but did not occur for either material B or material C.

Coercivity measurements are often used as a non-destructive measurement of the WC grain size. It could therefore be expected that the change in coercivity could be due to a change in WC grain size. However, the WC grain size did not differ significantly between the two different cooling rates for any of the materials. As described in section 2.1.1, the mean WC grain size is affected by the sintering time but that it is mainly affected by the milling conditions. The thermodynamic calculations showed that the slowly cooled samples were in liquid state for a longer time compared to the fast cooled samples. It could therefore be expected that the WC grain size would differ. Furthermore, all samples of each material were made of the same powder batch, hence have the same milling condition. This is probably the reason why the WC grain size between the different cooling rates is more or less constant within each material.

The cooling rate did not have a significant effect on the Co-m values for any of the materials. The variation of the Co-m values does not show any relation to the cooling rate and the difference between the values is probably due to aspects of the measurements rather than the cooling rate. The cooling rate of the sintering may affect the composition of the binder phase which could influence the coercivity. The Co-m measurement is an indirect measurement of the carbon content in the binder and does also give an indication of the amount of dissolved W in the binder. Since the results showed no significant difference in Co-m for the different cooling rates, the composition of the binder phase of these materials is probably not affected by the cooling rate. Hence, the change in coercivity of material A is likely not due to changes in binder composition.

The coercivity is also affected by the Co/WC interphase area. As mentioned in the results, the EBSD grain size distribution data of the Co binder phase for material A did not show the size distribution of the whole binder grains as expected but only the binder areas between the WC grains. However, this result is also useful since the coercivity is highly related to the Co/WC interphase area. The smaller binder areas between the WC grains, the more Co/WC interphase areas which result in higher coercivity. The results show that the size and fraction of Co binder areas between the WC grains is different in the slow cooled sample compared to the fast cooled sample of material A. The Co binder areas are smaller for the fast cooled sample, resulting in a larger Co/WC interphase area, which is indicated by both the EBSD image in Figure 13 and the statistics in Figure 12. The higher coercivity value for the fast cooled sample of material A can therefore be explained by the finer Co binder areas between the WC grains.

The size of the whole fcc-Co grains was also evaluated. The measurements were performed on a small area of the sample and showed only a few grains which yielded poor statistics. The

margin of error for this measurement is too large to draw any conclusions in this case. If there had been large differences between the samples, it would probably have been possible to see this even on the small areas measured and could give an indication of the difference in Co grain size. In this case, the differences between the samples were not significant and therefore no conclusion about the fcc-Co grain size could be drawn. However, since the fcc-Co grains are much larger than the Co areas between the WC grains, the effect of the fcc-Co grain size on the coercivity is probably smaller than the effect of the binder areas between the WC grains.

As stated in section 2.1.1, an increased sintering time results in an increase of the mean separation between the grains. The results of the thermodynamic calculations in this study showed that even though the holding time and sintering temperature were the same for all sintering cycles, the time at liquid state increases with decreasing cooling rate. Longer time at liquid-state implies that the material has more time for microstructural evolution. Therefore, the shorter time in liquid-state could be the explanation for the smaller mean separation between the WC grains (i.e smaller Co binder areas) for the fast cooled sample of material A.

Phase boundaries between the fcc and hcp Co phases also affect the coercivity, as described in section 3.2.1. The results in this study show that the hcp-Co grains are slightly smaller and that the area fraction is slightly larger for the fast cooled sample which leads to a larger interphase area between the hcp-Co and fcc-Co grains. This could also be an explanation for the increased coercivity. The result shows that the fraction fcc-Co changes with the cooling rate for material A, but for materials B and C there are no notable differences. The size of the fcc-Co areas are smaller for the fast cooling rate. Both the hcp-Co and fcc-Co are affected by the cooling rate, but a larger difference is seen for the fcc-Co. The difference in area fraction and size for the Co phases could be due to the prolonged time in liquid state.

One remaining question is why the differences in the size and fraction of the Co only occur in material A and not in material B or material C. One explanation could be that since materials B and C contain more Co, the mean free path of the Co is larger for materials B and C compared to material A and therefore comes closer to equilibrium during the sintering and are therefore not as affected by the cooling rate. Another difference between the materials is that material A has finer WC grains and this leads to more opportunity for nucleation of the binder phase at the surface of the WC grains and therefore yields finer Co grains. This may also lead to a larger mean free path of the Co binder.

In section 3.2.1 it is explained that the contiguity may affect the coercivity since it has been shown that materials with the same grain size but different contiguity results in different coercivity. The results in this study showed a slight increase in contiguity for the fast cooled sample for material A which also showed a higher coercivity at this cooling rate. Therefore, the higher contiguity could also affect the increased coercivity. Due to the standard deviation, it is not clear whether it is a relation between the cooling rate and contiguity for the different materials. It is therefore not possible to draw any conclusion about the effect of the cooling rate on the contiguity. Further investigation of the relation between the contiguity and the cooling rate is necessary to draw any conclusion.

The difference in contiguity between the different materials is more evident. In Figure 19, the standard deviation for 0.4°C/min is small and therefore it can be seen that there is a difference in contiguity between the different materials. This is also confirmed by the results of the different equations for the contiguity in Table 8. Material A clearly shows higher contiguity for all the different expressions. As explained in section 2.2.2, the contiguity decreases with increasing binder content. Since materials B and C has the same Co content and material A has a lower Co content, this could explain that the difference between materials A and B is larger than the difference between materials B and C.

There is also a difference between materials B and C, where B shows higher contiguity even if the Co content is the same for both materials. This could either be due to that the area fraction of Co (fcc+hcp) is slightly larger for material C and therefore has more Co/WC grain boundaries relative to WC/WC grain boundaries, hence lower contiguity. Material C also has a larger WC grain size which could also affect the contiguity. However, there is an ongoing discussion about whether the WC grain size affects the contiguity or not.

When investigating the etched samples in the LOM, spots of an unknown phase similar to  $\eta$ -phase were found in materials A and B that were sintered in the pilot-scale furnace. This was not found in the samples sintered in the production furnaces or the samples of material C with Cr additions. Since this unknown phase only appeared in the samples sintered in the pilot-scale furnace, it could be concluded that the contaminations were not present in the powder before the sintering. This led to suspicions that the unknown phase appeared due to contaminations in the pilot-scale furnace. When the phase was investigated with EDS in the SEM it was found that it contained around 30at% B. The contamination probably originates from the sintering of other materials in the pilot-scale furnace.

This phase was found late in the investigation and could therefore not be further examined. However, no significant difference was found when comparing the magnetic properties and the hardness values of the pilot-scale sintered samples of material A and B to the samples sintered in the production furnace. Therefore, the unknown phase does probably not cause any noteworthy changes in properties. The unknown phase was not found in any of the samples of material C. It is therefore reasonable to believe that the Cr impedes the formation of this phase.

The coercivity did not have as high an impact on the hardness as expected at the start of this investigation. The hardness usually increases with decreasing WC grain size. Since the coercivity is an indirect measurement of the WC grains size of the cemented carbide, one could expect that a higher coercivity value would imply higher hardness. The hardness did not change drastically with the coercivity. This is explained by that the WC grain size does not change with increased cooling rate. As seen in Figure 6a, there is a slight increase in hardness for the faster cooling rates for material A. However, this difference is not very large, only around 20 HV and the standard deviation for these measurements ranged between 4-15 HV. Therefore, it can not be stated that there is a connection between the hardness and the coercivity or the cooling rate.

## 6.1 Sources of Error

Even if the contiguity measurements with the line intercept method were carefully conducted the human factor is still a source of error. The line intercept method is based on interpretation and depending on who is performing the measurement, the microstructure may be interpreted differently. The magnification of the image of the microstructure also plays an important role. Higher magnification makes it easier to discriminate intercept types more accurately. It can be difficult to distinguish between a WC/WC grain and a small area of Co between two WC grains if the magnification is too low. Furthermore, these measurements were conducted on printed paper which also is a source of error since a printed picture often has a lower resolution than it has on the computer.

The contiguity calculation of material A was conducted on micrographs with the same magnification as the other materials that were more coarse-grained. It was therefore more difficult to distinguish the grain boundaries on the micrographs of material A than for materials B and C which could result in more incorrect measurements for this material. The calculations of the contiguity and the Co grain size are both three-dimensional properties but were both performed with the line intercept method on 2D micrographs. This is a source of error for these calculations. This error also applies to the EBSD analysis that also determines the grain size of a 2D map. To what extent the results are affected by this error is unknown since no calculations in 3D have been performed for comparison. However, these are all common methods and are mainly used for comparison and should therefore not affect the results significantly.

The Vickers hardness measurements were performed manually which cause an error of the human factor. This measurement is dependent on factors such as how the focus is set and how the one who performs the measurement interprets the image of the indentation. Hopefully, this systematic error is the same for all the measurements and does not affect the comparison of the different values.

For the EBSD analysis, one source of error could be the sample preparation. The EBSD measurements are very sensitive to irregularities on the surface. If the polishing is too rough, this could lead to an increased amount of zero solutions due to shadowing of the Co phase which cannot be indexed. The sample preparation can also lead to deformation leading to stresses in the atomic lattice which makes the detection with the EBSD more difficult. These factors could affect the results of the Co distribution. The results of the measurements of the fcc-Co grain size is very ambiguous since it was very hard to distinguish between the grains on the IPF images. The IPF images with different directions showed different grain boundaries. A comparison of all three directions (i.e x, y and x) was used when indicating the grain boundaries but it was still very difficult.

When it comes to the EDS analysis, this method should not be used for a light element such as boron which was done in this study. However, this was only used as an indication if boron was present or not. If an exact amount of an element is needed, a chemical analysis should be used.



### 6.2 Sustainability Aspect

Increased knowledge about how cemented carbides are affected by the cooling rate during sintering also contribute to production efficiency. Since it is known that the cooling rate does not have any notable effect on material B and C, these materials can be sintered with free cooling (i.e. 14°C/min) which is both energy and time-efficient. Therefore, this knowledge could lead to increased production efficiency.

This study also show that the cooling rate affects the coercivity of material A. With this knowledge it is easier to predict the properties and adjust the cooling rate to the desired coercivity. This may lead to less waste of sintered material with the wrong coercivity.

## 7 Conclusions

The aim of this work was to find an explanation as to why the contiguity increases with increased cooling rate for material A and if this phenomenon was found in other cemented carbide grades as well. The following conclusions were drawn from this study:

- The coercivity of material A increased with increasing cooling rate, the same behaviour was not found for material B and material C.
- The WC grain size did not affect the coercivity change as expected. The main contribution to the coercivity changes was the Co distribution.
- The fast cooled sample of material A had smaller Co areas between the WC grains which led to more Co/WC interphase area, resulting in an increased coercivity. The increased area fraction and decrease in grain size of the hcp-Co resulted in a larger hcp/fcc interphase area which probably also contributed to the increased coercivity. The changes of fraction and size of the Co is probably due to the time in liquid state during the sintering.
- Contiguity calculations with the line intercept method fits well with the contiguity calculated with equations based on binder volume fraction.
- The difference of contiguity between the different materials is mainly due to the fraction of Co. No conclusion about how the cooling rate affected the contiguity could be drawn since the standard deviation was large.
- An unknown phase similar to  $\eta$ -phase was found and probably appeared due to boron contaminations in the pilot-scale sintering furnace. It did not seem to have any significant effect on the properties investigated in this study.
- The hardness did not increase significantly with increased coercivity or cooling rate. This is probably due to the constant WC grain size.
- A method for determination of the fcc-Co grain size needs further development.

## 8 Future Work

For future investigations it would be interesting to study the relation between the magnetic properties and other sintering parameters than the cooling rate, such as the sintering temperature, gas flow etc. Especially for material B and C since these materials were not affected by the cooling rate.

The results in this study show a tendency for a increase in contiguity with increasing cooling rate during sintering. However, a more thorough investigation of the contiguity is needed to find if there is any relation between contiguity and the cooling rate. Contiguity measurement at several cooling rates and more measurement of the same sample would be needed for that investigation. The line intercept method could also be performed on EBSD images if the different grain boundaries are easier to define compared to the SEM images. Measurements on material A should also be performed at higher magnification to make it easier to distinguish between the grain boundaries. Further studies on the relationship between the WC grain size and the contiguity are also needed.

A more reliable method for fcc-Co grain size determination should also be developed. The information yielded from the EBSD-analysis should be enough to be able to distinguish between the different grains. These measurements should be done on as large maps as possible in order to include many fcc-Co grains and get better statistics.

The unknown phase similar to  $\eta$ -phase would also be interesting to study further. This could be done with chemical analysis to know the exact composition of the phase. This could give a better explanation to why it appears with B contaminations. A further study on how the boron dissolves into the samples and the source of the contaminations is also needed.

## 9 Acknowledgement

I am very glad that I got the chance to write my master thesis at Sandvik Mining and Rock Technology. It has been both challenging and educating but also very fun. Of course, all of the co-workers at SMRT deserves a thank you for the warm welcome that you gave me, but there are some people I would show some extra gratitude to. First and foremost, a huge thank you to my supervisor at Sandvik, Erik Östhols for all the time and effort that you put into my work. I would also like to express my sincere gratitude to both Ida Borgh and Mirjan Lilja who helped me with the SEM and EBSD analysis but also for contributing to valuable discussions. Also an extra thank you to Ida for all the help with the report. I would also like to thank Johanna Ankarsköld och Stefan Lind for all the help in the lab and Leif Åkesson for valuable discussions. Finally, I would like to thank my examiner at KTH, Greta Lindwall for the support during the project and for the help with the report.

## 10 References

- [1] J. García, V.C. Ciprés, A. Blomqvist, et al. “Cemented carbide microstructures: a review”. In: *International Journal of Refractory Metals and Hard Materials* 80 (2019), pp. 40–68. DOI: 10.1016/j.ijrmhm.2018.12.004.
- [2] X. Yi, X. Huang, C.-B. Liu, et al. “Effect of Cooling Rate on the Formation and Morphology of (W,V)C<sub>x</sub> in VC-doped WC–Co Cemented Carbide”. In: *Acta Metallurgica Sinica (English Letters)* 30 (Nov. 2016). DOI: 10.1007/s40195-016-0501-3.
- [3] A. Petersson. “Cemented Carbide Sintering: Constitutive Relations and Microstructural Evolution”. PhD thesis. KTH Royal Institute of Technology, 2004.
- [4] B. Uhrenius. *Powder Metallurgy*. Stockholm: KTH Royal Institute of Technology, 2000.
- [5] B. Kaplan, S. Norgren, M. Schwind, et al. “Reprint of “Thermodynamic calculations and experimental verification in the WC–Co–Cr cemented carbide system””. In: *International Journal of Refractory Metals and Hard Materials* 49 (2015), pp. 400–405. DOI: 10.1016/j.ijrmhm.2015.01.010.
- [6] C.H. Allibert. “Sintering features of cemented carbides WC-Co processed from fine powder”. In: *International Journal of Refractory Metals and Hard Metals* 19 (2001), pp. 53–61. DOI: 10.1016/S0263-4368(01)00004-X.
- [7] G. S. Upadhyaya. “CEMENTED TUNGSTEN CARBIDES Production, Properties, and Testing”. In: Westwood, New Jersey, USA: Noyes Publications, 1998. Chap. 5. Sintering Behaviour of Cemented Carbides.
- [8] L. Gu, J. Huang, and C. Xie. “Effects of carbon content on microstructure and properties of WC-20Co cemented carbides”. In: *International Journal of Refractory Metals and Hard Materials* 42 (2014), pp. 228–232. DOI: 10.1016/j.ijrmhm.2013.09.010.
- [9] I.-J. Shon, I.-K. Jeong, I.-Y. Ko, et al. “Sintering behavior and mechanical properties of WC–10Co, WC–10Ni and WC–10Fe hard materials produced by high-frequency induction heated sintering”. In: *Ceramics International* 35 (2009), pp. 339–344. DOI: 10.1016/j.ceramint.2007.11.003.
- [10] R. J. Cao, C. G. Lin, X. C. Xie, et al. “Determination of the average WC grain size of cemented carbides for hardness and coercivity”. In: *International Journal of Refractory Metals and Hard Materials* 64 (2017), pp. 160–167. DOI: 10.1016/j.ijrmhm.2016.12.006.
- [11] L. Sun, C.-C. Jia, and M. Xian. “A research on the grain growth of WC-Co cemented carbide”. In: *International Journal of Refractory Metals and Hard Materials* 25 (2007), pp. 121–124. DOI: 10.1016/j.ijrmhm.2006.03.002.
- [12] J. Weidow and H.-O. Andréén. “Binder phase grain size in WC-Co-based cemented carbides”. In: *Scripta Materialia* 63 (2010), pp. 1165–1168. DOI: 10.1016/j.scriptamat.2010.08.025.
- [13] B. Roebuck and E. A. Almond. “Deformation and fracture processes and the physical metallurgy of WC–Co hardmetals”. In: *International Materials Reviews* 33:1 (1988), pp. 90–112. DOI: 10.1179/imr.1988.33.1.90.

## 10 REFERENCES

---

- [14] G. S. Upadhyaya. “CEMENTED TUNGSTEN CARBIDES Production, Properties, and Testing”. In: Westwood, New Jersey, USA: Noyes Publications, 1998. Chap. 6. Microstructural Aspects of Cemented Carbides.
- [15] S. Luyckx and A. Love. “The dependence of the contiguity of WC on Co content and its independence from WC grain size in WC–Co alloys”. In: *International Journal of Refractory Metals and Hard Materials* 24 (2006), pp. 72–79. DOI: 10.1016/j.ijrmhm.2005.04.012.
- [16] V. T. Golovchan and N. V. Litoshenko. “On the contiguity of carbide phase in WC–Co hardmetals”. In: *International Journal of Refractory Metals and Hard Materials* 21 (2003), pp. 241–244. DOI: 10.1016/S0263-4368(03)00047-7.
- [17] B. Roebuck, K. P. Mingard, H. Jones, et al. “Aspects of the metrology of contiguity measurements in WC based hard materials”. In: *International Journal of Refractory Metals and Hard Materials* 62 (2017), pp. 161–169. DOI: 10.1016/j.ijrmhm.2016.05.011.
- [18] R. Warren and M. B. Waldron. “Microstructural Development During the Liquid-Phase Sintering of Cemented Carbides”. In: *Powder Metallurgy* 15:30 (1972), pp. 166–201. DOI: 10.1179/pom.1972.15.30.005.
- [19] K. G. Stjernberg. “Some relations between the structure and mechanical properties of WC–TiC–Co alloys”. In: *Powder Metallurgy* 13:25 (1970), pp. 1–12. DOI: 10.1179/pom.1970.13.25.001.
- [20] K. Herrman. “Hardness Testing - Principles and Applications”. In: ASM International, 2011. Chap. 1. The Fundamentals of Hardness Testing.
- [21] K. Herrman. “Hardness Testing - Principles and Applications”. In: ASM International, 2011. Chap. 2. Hardness Measurement of Metals - Static Methods.
- [22] K. P. Mingard, B. Roebuck, E. G. Bennett, et al. “Comparison of EBSD and conventional methods of grain size measurement of hardmetals”. In: *International Journal of Refractory Metals and Hard Materials* 27 (2009), pp. 213–223. DOI: 10.1016/j.ijrmhm.2008.06.009.
- [23] B. Roebuck. “Magnetic moment (saturation) measurements on hardmetals”. In: *International Journal of Refractory Metals and Hard Materials* 14 (1996), pp. 419–424. DOI: 10.1016/S0263-4368(96)00035-2.
- [24] B. Roebuck. *HARDMETALS Hardness and Coercivity Property Maps*. Teddington, Middlesex, England: National Physical Laboratory, 2002.
- [25] B. Roebuck. *Magnetic Coercivity Measurements for WC/Co Hardmetals*. Teddington, Middlesex, England: National Physical Laboratory, 1999.
- [26] Carbide Technology Inc. *What does Coercivity tell us?* Available at [www.carbidetechnologies.com/faq/what-does-coercivity-tell-us/](http://www.carbidetechnologies.com/faq/what-does-coercivity-tell-us/) (2020/09/16).
- [27] B. Roebuck. *A NATIONAL MEASUREMENT GOOD PRACTICE GUIDE No 20, Mechanical Tests for Hardmetals*. Teddington, Middlesex, England: National Physical Laboratory, 1999.
- [28] A. Bjerke. “Binder Migration in Double Pressed Drill Bit Inserts”. Lund University, 2017.

## 10 REFERENCES

---

- [29] Y. Leng. *Materials Characterization Introduction to Microscopic and Spectroscopic Methods*. Weinheim, Germany: Wiley, 2013, 2nd edition.
- [30] H. E. Exner. “Qualitative and Quantitative Interpretation of Microstructures in Cemented Carbides”. In: *Science of Hard Materials*. Boston, MA: Springer US, 1983, pp. 233–262. ISBN: 978-1-4684-4319-6. DOI: 10.1007/978-1-4684-4319-6\_14. URL: [https://doi.org/10.1007/978-1-4684-4319-6\\_14](https://doi.org/10.1007/978-1-4684-4319-6_14).
- [31] K. Carlsson. *Light Microscopy - Physics of Biomedical Microscopy*. Stockholm, Sweden: Applied physics Dept., KTH, 2007.
- [32] J.I. Goldstein, D.E. Newbury, J.R. Michael, et al. *Scanning Electron Microscopy and X-Ray Microanalysis*. Reading, Massachusetts: Springer US, 2003.
- [33] P. J. Goodhew, J. Humphreys, and R. Beanland. “Electron Microscopy and Analysis”. In: UK: Taylor and Francis Books UK, 2000. Chap. 5. The scanning electron microscope.
- [34] R. D. Holbrook, A. A. Galyean, J. M. Gorham, et al. “Chapter 2 - Overview of Nanomaterial Characterization and Metrology”. In: *Characterization of Nanomaterials in Complex Environmental and Biological Media*. Vol. 8. Frontiers of Nanoscience. Elsevier, 2015, pp. 47–87. DOI: <https://doi.org/10.1016/B978-0-08-099948-7.00002-6>.
- [35] G. C. Wang. “5 - Slag processing”. In: *The Utilization of Slag in Civil Infrastructure Construction*. Woodhead Publishing, 2016, pp. 87–113. DOI: 10.1016/B978-0-08-100381-7.00005-7.
- [36] B. Roebuck and E. G. Bennett. “Phase size distribution in WC/Co hardmetal”. In: *Metallurgy* 19 (1986), pp. 27–47. DOI: 10.1016/0026-0800(86)90005-4.
- [37] H. E. Exner and H. F. Fischmeister. “Structure of sintered tungsten carbide-cobalt alloys”. In: *Arch. fur Eisenhuttenwesen* 37 (1966), pp. 417–426. DOI: 10.1002/srin.196602777.
- [38] H.-O. Andrén. “Microstructures of cemented carbides”. In: *Materials & Design* 22.6 (2001), pp. 491–498. DOI: [https://doi.org/10.1016/S0261-3069\(01\)00006-1](https://doi.org/10.1016/S0261-3069(01)00006-1).
- [39] Sandvik AB. *Internal routine*. 2020.
- [40] I. Borgh. “On the three-dimensional structure of WC grains in cemented carbides”. In: *Acta Materialia* 61 (2013), pp. 4726–4733. DOI: 10.1016/j.actamat.2013.05.008.
- [41] F. Josefsson. “Development of a quantitative method for grain size measurement using EBSD”. KTH Royal Institute of Technology, 2012.
- [42] A. Nordgren. *Sandvik internal method*.
- [43] Sandvik AB. *Internal database, version 2018*.

## Appendix A - Magnetic Measurements

Charge no.	Cooling rate	Coercivity [kA/min]		
		Material A	Material B	Material C
CH521	free cooling	12.53	6.193	5.710
CH520	free cooling	12.6	6.215	5.683
CH505	8 deg/min	12.44	6.078	-
CH509	8 deg/min	-	-	5.606
CH514	8 deg/min	12.44	6.143	5.633
CH523	5 deg/min	12.36	6.160	5.628
CH516	5 deg/min	12.35	6.211	5.584
CH504	2 deg/min	11.96	6.117	-
CH510	2 deg/min	12.10	6.234	5.65
CH517	1.4 deg/min	11.96	6.195	5.634
CH522	0.8 deg/min	11.66	6.155	5.610
CH513	0.8 deg/min	11.62	6.209	5.605
CH507	0.8 deg/min	11.53	6.231	-
CH506	0.4 deg/min	11.14	6.083	-
CH511	0.4 deg/min	11.32	6.131	5.533
CH519	0.4 deg/min	11.29	6.149	5.560
prod	-	11.31	6.032	-
prod	-	11.95	6.239	5.566

Figure 20: Measured coercivity values for each sintering charge for each material.



Co-m [%]				
Charge no.	Cooling rate	Material A	Material B	Material C
CH520	free cooling	5.537	10.37	8.391
CH521	free cooling	5.594	10.42	8.441
CH514	8 deg/min	5.535	10.34	8.287
CH509	8 deg/min	-	-	8.222
CH505	8 deg/min	5.544	10.34	-
CH516	5 deg/min	5.520	10.33	8.170
CH523	5 deg/min	5.573	10.39	8.340
CH510	2 deg/min	5.515	10.34	8.316
CH504	2 deg/min	5.566	10.38	-
CH517	1.4 deg/min	5.551	10.37	8.360
CH507	0.8 deg/min	5.454	10.27	-
CH513	0.8 deg/min	5.498	10.31	8.168
CH522	0.8 deg/min	5.566	10.39	8.419
CH511	0.4 deg/min	5.498	10.32	8.360
CH506	0.4 deg/min	5.529	10.33	-
CH519	0.4 deg/min	5.552	10.37	8.407
prod	-	5.553	10.35	-
prod	-	5.504	10.38	8.243

Figure 21: Measured Co-m values for each sintering charge for each material.

## Appendix B - Vickers Hardness Values

HV20				
Charge no.	Cooling rate	Material A	Material B	Material C
CH520	free cooling	1512	1170	1117
CH521	free cooling	1502	1169	1118
CH505	8 deg/min	1537	1183	-
CH509	8 deg/min	-	-	1124
CH514	8 deg/min	1512	1164	1134
CH516	5 deg/min	1506	1165	1128
CH523	5 deg/min	1517	1165	1116
CH504	2 deg/min	1518	1158	-
CH510	2 deg/min	1507	1156	1129
CH517	1.4 deg/min	1494	1167	1113
CH507	0.8 deg/min	1499	1160	-
CH513	0.8 deg/min	1493	1174	1123
CH522	0.8 deg/min	1503	1157	1110
CH506	0.4 deg/min	1492	1173	-
CH511	0.4 deg/min	1493	1165	1113
CH519	0.4 deg/min	1497	1156	1100
prod	-	1485	1146	-
prod	-	1507	1170	1120

Figure 22: Measured hardness values for each sintering charge for each material.

# Appendix C - Contiguity Values

Contiguity			
Cooling rate	Material A	Material B	Material C
free cooling	0.70	0.46	0.41
(14 deg/min)	0.67	0.55	0.42
	0.73	0.43	0.39
5 deg/min	0.60	0.53	0.43
	0.68	0.48	0.34
	0.63	0.52	0.48
0.4 deg/min	0.67	0.51	0.32
	0.65	0.50	0.34
	0.62	0.47	0.33
Production	0.62	0.48	0.36
	0.68	0.49	0.43
	0.60	0.53	0.51

Figure 23: Contiguity values for the three different cooling rates of each material.

TRITA ITM-EX 2021:04